KANSAS GEOLOGICAL SURVEY
OPEN-FILE REPORT 1995-58

A High-frequency Ground-penetrating Radar Study
of the Plattsburg Limestone and Bonner Springs Shale,
I-435/I-70 Interchange, Southwest Wyandotte County, Kansas

by

Alex Martinez
Joseph M. Kruger
Evan K. Franseen
Mike L. Shoemaker
Michael S. Roark

Disclaimer

The Kansas Geological Survey does not guarantee this document to be free from errors or inaccuracies and disclaims any responsibility or liability for interpretations based on data used in the production of this document or decisions based thereon. This report is intended to make results of research available at the earliest possible date, but is not intended to constitute final or formal publications.

Kansas Geological Survey
1930 Constant Avenue
University of Kansas
Lawrence, KS 66047-3726

A High-Frequency Ground-Penetrating Radar Study of The Plattsburg Limestone and Bonner Springs Shale, I-435/I-70 Interchange, Southwest Wyandotte County, Kansas

Kansas Geological Survey Open File Report 95-58

Alex Martinez[1], Joseph M. Kruger[1], Evan K. Franseen[1],
Mike L. Shoemaker[2], Michael S. Roark[2],

[1]Kansas Geological Survey, Lawrence, KS
[2]University of Missouri-Rolla, Rolla, MO

INTRODUCTION

A pilot study to determine the usefulness of high-frequency ground-penetrating radar (GPR) methods in delineating geometries, erosional truncation surfaces, and internal bedding features within carbonate and clastic strata was undertaken in the Spring of 1995. High-frequency ground-penetrating radar methods are capable of resolving subsurface features in great detail. These methods have the potential of allowing internal geometries and bedding features of rock units to be studied beyond outcrop faces and adding stratigraphic information to databases where outcrop information is limited.

The study site for this report is located in southwest Wyandotte County, Kansas (Fig. 1) on the northeast access ramp of the I-435/I-70 interchange (stop 4 of Watney et al., 1989) (Figure 2). Three profiles of GPR data, with a total line length of 1 km, were gathered at this site. These data were acquired to determine the capabilities of GPR to image stratigraphic features associated with the Bonner Springs Shale, which caps the Wyandotte depositional sequence (Watney et al., 1989), and the Merriam Limestone, a member of the Plattsburg Limestone which forms the basal portion of the subjacent Plattsburg depositional sequence (Watney et al., 1989). The specific features of interest in these units include: 1) hemi-channel forms within the sandstone lithology of the Bonner Springs Shale, 2) the erosional contact between the Merriam Limestone and Bonner Springs Shale, and 3) internal bedding geometries in the sandstone lithology of the Bonner Springs Shale and within the Merriam Limestone.

GEOLOGIC SETTING

The Bonner Springs Shale contains a variety of lithologies, as is typical of the thicker deltaic outside shales. However, at the study site the exposures provide an unusual opportunity to examine features not normally preserved at the top of a sequence on the shelf. The Bonner Springs at the study site consists of up to 8.7 m (29 ft) of channel sandstone overlain by 1 m (3.3 ft) of sandy shale evidencing multiple episodes of erosional scouring and backfilling. The sandstone is extensively ripple cross-laminated with a few festoon sets and local climbing ripple-drift cross-lamination and herringbone crossbedding developed at the base (Enos et al., 1989). The sandstone contains a few brachiopods, pectins, and gastropods. The overlying shale contains fenestrate bryozoans and unidentified shell fragments in addition (Enos et al., 1989). This sandstone, which apparently eroded the entire Bonner Springs Shale, is truncated by a distinct hemi-channel form (section X; Figs. 2 and 3) that is filled with silty shale; silty, pebbly sandstone; and shale; it extends to the fossiliferous shale beneath the Merriam in sections VIII and IX (Enos et al., 1989)

(Figs. 2 and 3). This hemi-channel form sand/shale sequence is truncated by another hemi-channel form expressed as abrupt westward thickening of the Merriam Limestone from 0.9 m (3 ft) in section IX to 4.0 m (13 ft) in section X (Enos et al., 1989) (Figs. 2 and 3).

The Merriam Limestone is the flooding unit of the Plattsburg sequence (Watney et al., 1989). Lithologically, the basal part is typically a packstone, but ranges from very argillaceous, nodular-weathering yellow limestone to ooid grainstone. The middle portion of the bed, below the most prominent shale break, is typically a skeletal packstone containing prominent coated grains or oncoids (Enos et al., 1989). An overlying shale bed or parting can be traced over most of the area. The top unit is one or two beds of skeletal packstone. Oncoids are locally prominent. Argillaceous limestone caps are developed locally. Biotic constituents include *Composita* brachiopods, crinoid columnals, gastropods, productid brachiopods, fenestrate bryozoans, fusulinids, bivalves, phylloid algae, spiriferid brachiopods, ramose bryozoans, echinoid fragments, brachiopod spines, solitary corals, encrusting bryozoans, pectins encrusting worms , encrusting foraminifera, large scaphopods, and rarely, trilobites; burrows are prominent at the top (Enos et al., 1989).

The upper surface of the Bonner Springs Shale, in surrounding areas where the typical shale lithology is present, contains evidence of subaerial exposure (Watney et al., 1989). This subaerial exposure surface is the sequence boundary between the Wyandotte sequence and the overlying Plattsburg sequence. The Bonner Springs sandstone channel-fills at the study site are traditionally correlated with the more normal lithologic expressions of the Bonner Springs Shale, and are included in the upper portion of the Wyandotte sequence (e.g. Watney et al., 1989). However, at the study site, the channel-fills in the Bonner Springs and the overlying Merriam Limestone all contain marine fossils. In addition, the distinct hemi-channel form (section X; Figs. 2 and 3) that is filled with silty shale, silty pebbly sandstone, and shale, and extends to the fossiliferous shale beneath the Merriam, also locally contains some transported calcareous (caliche) nodules. These caliche nodules were likely derived from the subaerial exposure surface at the top of the Bonner Springs Shale from the immediately surrounding areas. This evidence suggests that the Bonner Springs hemi-channels were incised after subaerial exposure of the Bonner Springs Shale and that the sandstones and sandy shales within the hemi-channels were deposited during the subsequent marine transgression. The marine transgression continued as evidenced by the transition to limestone deposition of the overlying Merriam Limestone. Therefore, from a sequence stratigraphy standpoint, it seems more reasonable to include the Bonner Springs sandstone channel-fills as part of the basal portion of the Plattsburg sequence instead of the upper portion of the Wyandotte sequence. The recurring channel forms, marine sediments, and some of the sedimentary features (e.g. herringbone crossbedding) in the Bonner Springs sandstone and Merriam Limestone are likely best explained by tidal currents that responded to antecedent topography developed in large part by algal banks in the Wyandotte Formation. This

paleotopography likely resulted in lateral funneling of currents and formation of channels in relative bathymetric lows (Watney et al., 1989). This interpretation is similar to the processes invoked by Cunningham and Franseen (1992) during deposition of the overlying Captain Creek Limestone at the base of the Stanton sequence.

GPR METHODS, DATA COLLECTION, AND PROCESSING

Methods

Ground-penetrating radar (GPR) is a high-resolution near-surface geophysical technique that uses antennas to send electromagnetic pulses into the ground in order to image the subsurface via returned reflection energy. Similar to seismic reflection methods, where reflections are caused by boundaries associated with acoustical impedance contrasts, GPR reflections are caused by the electromagnetic waves encountering media of different electrical properties - namely boundaries consisting of a contrast in the dielectric constant of the material above and below the boundary. Values for dielectric constants (K) range from 1 for air, 3-5 for dry sand, 4-8 for limestone, 5-13 for shale, 5-40 for clay, and 81 for water (Davis and Annan, 1989). Dielectric constant values affect the velocity of electromagnetic waves through a material, and are related to velocity in non-magnetic materials by:

$$\text{velocity} = \frac{c}{\sqrt{K}}$$

where $c = 3 \times 10^8$ m/s (speed of light in a vacuum). Using the relationship given above, one-way velocities for materials range from 0.3 m/ns (meters/nanosecond) for air, 0.134-0.173 m/ns for dry sand, 0.11-0.15 m/ns for limestone, 0.077-0.134 m/ns for shale, 0.047-0.134 m/ns for clay, and 0.033 m/ns for water. Antenna frequencies typically range from 10 MHz to 1000 MHz (a 500 MHz antenna was used in this study), and imaging resolution is proportional to antenna frequency, whereas penetration depth is inversely proportional to antenna frequency (the greater the antenna frequency, the less penetration but greater detail). Vertical resolution varies from 1-1.5 m (3-5 ft) for low-frequency antennas (10-100 MHz), to 0.02-0.3 m (1-12 in) for high-frequency antennas (500-1000 MHz) for most materials (Davis and Annan, 1989).

GPR profiles have a similar appearance to seismic profiles, and usually are represented as common depth point (cdp) data, with amplitude variations representing differences in reflection energy. As with seismic data, vertical scales are in time (or depth if the data have been depth migrated), whereas lateral scales are in distance. However, the scales differ by several orders of magnitude; GPR records have lengths measured in nanoseconds (1×10^{-9} s), compared to

milliseconds ($1x10^{-3}$ s) in seismic records. Also, the distances between cdps in GPR profiles are usually much smaller than seismic profiles (an average GPR cdp spacing of 3 cm for this study, versus standard, near-surface seismic reflection cdp spacing of 0.3-1.5 m for high-resolution profiles).

Equipment & Data Collection

Preparation of the study site included clearing the antenna path of major obstructions such as large rocks (or moving the line when that was not possible), flagging stations along the antenna path, collecting relative elevation information for the stations, and obtaining photomosaics of the outcrops in relation to the stations. The pathway remained as close to the roadcut face as possible to facilitate correlation with the exposed geology and to take advantage of the thin soil cover in this area (Fig. 2). However, due to the presence of trees, brush, and a terraced outcrop face, the southern and western parts of the profile were moved farther away from the rock face. Station flagging at a 3.0 m (10 ft) interval served several purposes. It assisted in retaining the same antenna pathway for each of the various scan lengths (record lengths) collected. It also allowed correlation of the GPR data with specific ground locations via photomosaics, and aided in control of antenna velocity during data collection to ensure even cdp coverage. The collection of relative elevation information from stations every 15.2 m (50 ft) allowed the data to be corrected for elevation differences during processing. These corrections immensely aided the interpretation of reflection information and correlation with outcrop information. Elevations were obtained using a level and rod with an accuracy to within $\pm$ 3 cm. The photomosaics were also gathered in increments of 15.2 m (50 ft) to allow correlation between the outcrop and GPR data. The antenna pathway behind the road cut was a relatively smooth, grassy surface of varying soil thickness.

The equipment used for the study was a GSSI SIR System-8 GPR unit, with a DT6000A tape unit and 500-MHz dominant-frequency antenna. Scan lengths of 40, 60, and 80 ns were recorded at a rate of 12.8 scans/second as the antenna was pulled along the line three times in order to experiment with data quality. The equipment was placed within a large-wheeled garden cart, which allowed continuous profiling along the entire line for each scan length. Only the 60 ns data is presented in this report because it generated higher resolution data than the 80 ns scan; there were reflections visible in some areas below 40 ns, and very little, if any, reflectivity was recorded below 60 ns. The tape unit recorded coherent system noise beginning at approximately 40 ns on each trace. This noise masked most of the reflection information below 40 ns, greatly reducing the signal-to-noise ratio of the longer scans. Digital filtering of the data removed some, but not all, of the noise. A short marker-pulse was recorded whenever a flagged station was passed (every 3.0 m; 10 ft), and a double pulse was recorded at every fifth flag (every 15.2 m; 50 ft). This enhanced

control over how fast the antenna was pulled along the ground, and allowed correlation between the data and the outcrop.

Data Processing

The data were downloaded from the DT6000A tape unit and converted from RADAN format into 4-byte SEGY format before importation into Seismic Unix (SU) on a workstation. Once within SU, the data were time- and distance-scaled by a factor of $1x10^6$ for viewing and processing purposes. The 60 ns scan data had 512 samples per trace, a sample interval of 0.117 ns, and a lateral distance (cdp trace spacing) of approximately 3 cm per trace.

The GPR data were treated as stacked seismic reflection data within SU, opening up the possibility of post-stack digital processing. A generalized data processing flow for the GPR data is shown in Figure 4. Front-end mutes removed high-amplitude first arrivals, allowing trace balancing to enhance low-amplitude reflection information recorded later in the data. Coherent noise filtering removed most of the lateral system noise recorded in the regions below 40 ns in the data. Bandpass and frequency-wavenumber (f-k) filters reduced the lower frequency information and enhanced high-frequency reflections. Trace balancing via automatic gain controls (AGC) allowed some of the low-amplitude events to become more visible. The data were then elevation corrected to an arbitrary datum at the highest elevation along the line to prevent the loss of data and remove the longer period elevation static shifts that inhibit correlation with the outcrop. Therefore, the top of the data on the GPR sections roughly corresponds to the surface.

RESULTS

General Results

A site map of the study area shows the relationship between the GPR line and the outcrop (Fig. 2). The GPR data and photomosaics are shown in Figures 5 and 6 respectively. Station locations on the photomosaics are indicated by survey crew members holding station number signs while standing on the stations. The stations are indicated on the GPR data by vertical pulse lines on the sections every 3.0 m (10 ft) and double lines every 15.2 m (50 ft). The data are plotted down to 50 ns below the surface. This corresponds to a depth of 3.0 m (10 ft) assuming an average one-way velocity of 0.12 m/ns (0.4 ft/ns), which is appropriate for limestone (Davis and Annan, 1989). Uninterpreted copies of the GPR data and outcrop photomosaics shown in Figures

5 and 6 are located in Appendix A.

Although data were collected along the entire 366 m (1200 ft) profile, only the data acquired between stations 0 and 400 (Fig. 2) are usable. The lack of reflectivity on the remainder of the data is probably due to higher signal attenuation caused by the thicker soil cover, the conductive shale, a high content of conductive clays in the Bonner Springs sandstones and siltstones, or a lack of dielectric constant contrasts in the underlying rock units. Because of the signal loss or lack of reflectivity, the GPR fails to fully image the erosional hemi-channel features and internal bedding characteristics within the Bonner Springs sandstone lithologies in areas where those features are visible on the outcrop. Only a relatively thin, hemi-channel form within the Bonner Springs Shale is imaged by the GPR data. However, the GPR data did image the top and base of the Merriam Limestone, and many internal bedding planes and other features within the Merriam Limestone member.

Along the northern and eastern portion of the GPR profile, where the data are usable, high amplitude coherent reflections are correlated with major unit boundaries on the outcrop and are indicated by the heavy dashed lines (Figs. 5 and 6). These reflections break the Merriam Limestone into five major reflective packages or units (ML1-ML5). In addition, GPR is locally successful at imaging internal bedding features within the Merriam Limestone. Reflections within the major packages are identified by thin dashed lines and are correlated as closely as possible with bedding planes visible on the outcrop. A transition (in a stratigraphically older direction) from limestone to shaly limestone to limestone beds is observed in the Merriam Limestone between stations 0 and 400 (Fig. 6). This transition is also indicated by changes in the internal reflectivity of packages ML1-ML5 (Fig. 5). Units ML1, ML2, and ML5 appear to represent the limestone beds, whereas ML4 and much of ML3 represent the shaley limestone beds (Fig. 6). These units are generally flat lying between stations 0 and 280, but increase in dip between stations 280 and 400 as the margin of a series of hemi-channels is approached. This dip is mostly primary because the beds were deposited along the flanks of a channel. Primary dip is also indicated by flatter dips of overlying and underlying strata in some cases. However, the increased dip may be partially related to compaction of underlying finer grained clastic units such as shale, which would exaggerate the primary dip. Although an exact correlation between a given reflection and a given bedding surface may not be possible in all cases due to a lack of precise depth control on the GPR sections, the overall geometries indicated by the GPR interpretation correlate quite well with the outcrop data.

Correlations between true reflections and the outcrop are complicated by instrument generated noise which created events that are parallel to the top of the GPR data (elevation corrected surface) and extend downward throughout the data. Because of the AGC operator applied during processing, this noise is particularly apparent where the reflective signal is weak or

nonexistent. It is generally easy to ignore the noise when it cuts across the true reflections, but it complicates interpretation where it is parallel or subparallel to the reflective fabric. Another complicating factor for interpretation is the waviness of the reflectivity with lateral spatial wavelengths on the order of less than a foot to tens of feet in some areas (Fig. 5). This characteristic may be caused by a variety of factors, including elevation statics which were unaccounted for due to variations in soil velocity or minor elevation changes between the surveyed station locations, wavy bedding in the limestone, or intersecting diffractions (convex upward hyperbolas) caused by joints or fractures in the limestone (Fig. 6).

Unit ML1

A distinct limestone bed just under the present day land surface (ML1) is clearly imaged by GPR. The top of this bed is traceable between stations 120 and 265 whereas the base is imaged between stations 20 and 300 (Figs 5 and 6). Both the upper and lower contacts of this approximately 1 m (3 ft) thick bed are imaged as relatively high amplitude reflections by GPR along most of its lateral trace. Internal reflections are seen, but are generally of lower amplitude than the top and base. They are also of low amplitude when compared to the internal reflectivity of lower limestone units. The reflection character of ML1 is likely due to the relatively massive bedding character and homogenous limestone lithology of this unit compared to underlying, thinner bedded strata. This results in a relatively large dielectric constant contrast between ML1 and adjacent beds, compared to small differences in dielectric constants internally.

The relatively large reflection amplitude of the top of ML1 may indicate that it is the contact between the Merriam Limestone and overlying Hickory Creek Shale (Fig. 3). It is also possible that the reflection represents the base of a thicker soil layer, potentially a residual from the Hickory Creek Shale. The low velocity nature of this overlying material is indicated by the slight velocity pull-down between stations 145 and 250 (Fig. 5).

Prominent diffractions also occur within and along the top of this unit. Some good examples of these are near the surface between stations 65 and 90, and one near the top of the unit at station 150 (Fig. 5) where there appears to be some collapse as indicated by the abrupt thinning between stations 145 and 150. These diffractions are probably due to soil or air-filled joints or other fractures in the limestone beds. The wider the fracture, or the more air it contains, the better the diffraction. This interpretation is supported by the presence of joints or other fractures on the outcrop (Fig. 6).

Unit ML2

Unit ML2 is not as massively bedded as ML1 but is still a fairly competent limestone (Fig. 6). This unit can be traced from approximately station 20 to station 315. Large amplitude reflections within this unit (Fig. 5) are probably due to a greater amount of argillacious material between the limestone beds or compaction differences at bed boundaries, creating a relatively large contrast in the dielectric constants between the two lithologies. The good signal penetration through unit ML2 suggests that most of the unit is composed of limestone.

Gradual thickening and thinning of beds within unit ML2 is indicated on both the GPR data (Fig 5) and the photomosaics (Fig. 6). However, exact correlations between the two data sets is not possible in most cases. This may be due to lateral velocity changes within the rock units or changes in thickness both into the outcrop as well as along it. Another limiting factor may be the resolution of the data. Although the data show resolutions on the order of a few decimeters, the variations in thickness may be subtle enough that the wavelength of the data is too large to resolve them. The thickness variations may also occur gradually enough laterally that the noise in the GPR data overrides any changes that may occur in the signal. One exception to this is the termination of the uppermost internal reflection near the top of unit ML2 between stations 220 and 230 (Fig. 5), which correlates with the thinning of a bed between this reflection and the top of ML2. This reflection is characterized by a fairly high amplitude trough (white) with relatively high amplitude adjacent peaks (dark gray) along most of its length between stations 20 and 170. The relative strength of this reflection dies out gradually between stations 170 and 190, with the reflection varying between a single event and a doublet beyond station 190 as it interferes with the reflection associated with the top of ML2. Eventually this event dies out between stations 220 and 230 as the bed becomes too thin to image with the GPR data.

Unit ML3

The top of unit ML3 is well imaged between stations 30 and 315 (Fig. 5). This is probably due to the large dielectric constant contrast between the lowermost limestone bed in unit ML2 and the more argillacious limestone near the top of ML3. The weathering pattern of this unit suggests that it is predominantly a thin-bedded shaly limestone which becomes more argillaceous downward (Fig. 6). The downdip traces of these beds die out at shallower depths compared to the underlying and overlying relatively purer carbonate units (Fig. 5). The higher clay content of this unit may be why we see relatively little internal reflectivity and why the base of it is imaged for only a short distance as it approaches the surface between stations 320 and 330 (Fig. 5).

Unit ML4

Unit ML4 is a shaley limestone, and is even more argillaceous and thinner bedded than the overlying unit. This is indicated by its recessive weathering nature in outcrop (Fig. 6). Reflections from this unit are only imaged near the surface between stations 320 and 360. As in unit ML3, reflections associated with ML4 are relatively weak and die out at rather shallow depths, probably due to the higher clay content of the unit, the lack of significant dielectric constant contrasts, and the thin bedding (Fig. 5). The presence of this unit also causes so much signal attenuation that the reflections associated with the underlying competent limestone (ML5) die out rapidly beneath it.

Steeply dipping events within unit ML4 occur near the surface around station 340 (Fig. 5). These events appear to be diffractions, possibly from open fractures near the surface. They may also be due to the edges of collapse features or increased weathering in this relatively easily eroded unit.

Unit ML5

Unit ML5 is primarily a thin-to medium-bedded limestone similar to unit ML2. It is a fairly resistant unit and is easily visible in outcrop between stations 270 and 400 (Fig. 6). This unit is imaged on the GPR between stations 355 and 400 (Fig. 5). The top of ML5 is a relatively strong reflection, but dies out down dip due to signal attenuation caused by the overlying shaly limestone of unit ML4. Strong internal reflections are also present within unit ML5, (Fig. 5). These reflections also die out down dip due to signal attenuation from unit ML4. The internal reflections are particularly strong as they approach the surface between stations 375 and 390. As with unit ML2, the high amplitude reflectivity at bed boundaries is probably due to changes in clay content or compaction. Diffractions appear to occur along many of the bed boundaries in unit ML5 and are most apparent close to the surface. Prominent diffractions are found along the uppermost internal reflection indicated on the GPR data between stations 355 and 370. As with the diffractions in unit ML2, these diffractions are probably caused by open or soil-filled joints and other fractures near the surface, or possibly the edges of collapse features in some locations.

The base of this unit is an erosional contact between the Merriam Limestone and underlying Bonner Springs Shale. A hemi-channel form for the contact is supported by the westward thickening of the Merriam Limestone that is visible on the outcrop (Fig. 6), the GPR data (Fig. 5), and the measured sections (Enos et al., 1989) (Figs. 2 and 3).

Unit BS1

GPR is successful to a limited extent in imaging the erosional contact (hemi-channel form) between the Bonner Springs silty shale-shale lithology (BS1) and the overlying Merriam Limestone (ML5). The contact is visible on both the outcrop and GPR profile between stations 360 and 400. This area of the profile is where measured section IX is located (Figs. 2 and 3). The contact is expressed on the outcrop by the low angle truncation of dipping shale, silty shale, silty limestone, and siltstone layers in the Bonner Springs Shale (BS1) by the overlying Merriam Limestone (ML5) (Fig. 6). This unit correlates with the distinct siltstone and shale filled hemi-channel form below the Merriam Limestone and above channel filling sandstones and siltstones (measured sections VIII, IX, and X in Figures 2 and 3). This hemi-channel form is also supported by a very gradual thickening of unit BS1 downdip (Fig. 6). This thickening also appears to be indicated on the GPR data but with less certainty (Fig. 5). On the GPR data, the contact between the Bonner Springs Shale and Merriam Limestone is a relatively high amplitude reflection, but no more reflective than those between limestone beds in the overlying ML5 unit (Fig. 5). Unit BS1 is also relatively thin, so its base is only a few cycles below the top. Although the erosional truncation of beds is apparent on the outcrop, the terminations of BS1 beds against the Merriam Limestone are at too low of an angle to see on the GPR data.

Unit BS2

The top of BS2 is also an erosional contact with a hemi-channel form that cuts across flatter lying beds below (Fig. 6). This unit correlates with the lower channel filling sandstone and siltstone in measured sections VIII, IX, and X (Figs. 2 and 3), which occurs below the siltstone and shale filled hemi-channel form above. The upper contact is quite obvious on the outcrop, but it is much less so on the GPR data (Fig. 5). The relatively flat-lying beds of siltstone, shaley siltstone, sandy siltstone, and sandstone, are not even imaged on the GPR data. The poor reflectivity along the top of unit BS2, as well as within this unit, is probably due to signal attenuation caused by the argillacious nature of the siltstones and sandstones in unit BS2, the silty to shaley layers in the overlying unit (BS1), or a lack of dielectric constant contrasts within the siltstones of BS2.

CONCLUSIONS

High-resolution ground-penetrating radar was successful in imaging the Merriam Limestone Member. However, this technique was mostly unsuccessful in imaging depositional features within the Bonner Springs Shale. The lack of signal penetration in the Bonner Springs units is likely due to the argillaceous nature of the sandstones, siltstones, and shales within the Bonner Springs Shale, combined with a relatively high clay content and thickening of the soil in the area of the profile where the Bonner Springs Shale is exposed. A lack of dielectric constant contrasts within much of the Bonner Springs units may also contribute to the paucity of reflections.

The reflectivity within a limestone unit depends on the lithologic changes within that unit. Thick-bedded limestones with little change in lithology within beds show little internal reflectivity. Medium-to thin-bedded limestone units show a very strong internal reflectivity when bed thicknesses are comparable to the dominant wavelength of the reflected GPR signal, and lithologic changes occur between the beds (e.g. more argillaceous between beds). These internal reflections can be traced over relatively great lateral distances. As a bed thins, reflections from its top and base may begin to interfere with reflections from adjacent beds, causing constructive or destructive interference. A single cycle reflection associated with the bed may then turn into a doublet and terminate completely if the bed becomes thin enough. Shaley, thin-bedded limestones, show little internal reflectivity and cause fairly rapid GPR signal attenuation.

Joints, fractures and possibly collapse features within limestone units are imaged by GPR as diffractions. These are particularly visible near the top of more competent limestone beds close to the surface, and are probably related to soil, air, or a more argillaceous unit above filling the voids. Intersecting diffractions may add to the waviness of reflections within limestones. However, the waviness may also be caused by short period static shifts or waviness along the surface of the bed.

High-resolution GPR is an excellent tool for imaging the internal stratigraphy of limestones, provided that high-conductivity soils or rock units above the limestone do not significantly attenuate the signal. Full-wavelength resolution with this technique is on the order of a few decimeters (depending on the velocity of the unit), and penetration depths can reach up to 3 m (10 ft) or more. High-resolution GPR is also useful for imaging the near-surface structure of limestones, as indicated by the transition from dipping to relatively flat beds along the profile. These aspects suggest that GPR can be used to extend stratigraphic and structural information from a limestone unit into the outcrop, and if needed, create a grid of data to achieve a 3-D image of the unit in question. The correlations between geology and GPR in this report also suggest that GPR can be used as a remote sensing tool, even when outcrop information is sparse or unavailable.

ACKNOWLEDGMENTS

We would like to thank Dr. Neil Anderson from the University of Missouri-Rolla, for the use of UMR's GPR equipment. We would also like to thank David Leck for assisting in GPR data collection, and Tim Carr for making Kansas Geological Survey funds available for the survey.

REFERENCES

Cunningham, K.J. and Franseen, E.K., 1992, Conglomeratic Limestones of the Upper Pennsylvanian Captain Creek Limestone and Their Association with the Lower Sequence Boundary of the Stanton Depositional Sequence, Northwestern Johnson County, Kansas: Kansas Geological Survey Open-File Report 92-51, 47 p.

Davis, J. L. and Annan, A. P., 1989, Ground-Penetrating Radar for High-Resolution Mapping of Soil and Rock Stratigraphy: Geophysical Prospecting 37, 531-551.

Enos, P., Herman, D., Watney, W.L., and Franseen, E., 1989, Stop 4 I-70/I-435 Interchange: Bonner Springs Shale and Plattsburg Limestone: *in* Watney, W.L., French, J.A., and Franseen, E.K., eds., 1989, Sequence Stratigraphic Interpretations and Modeling of Cyclothems in the Upper Pennsylvanian (Missourian), Lansing and Kansas City Groups in Eastern Kansas: Kansas Geological Society Guidebook, 41st Annual Field Trip, October 14-15, 1989, Kansas Geological Survey Open-File Report 89-44, p 115-126.

Watney, W.L., French, J.A., and Franseen, E.K., eds., 1989, Sequence Stratigraphic Interpretations and Modeling of Cyclothems in the Upper Pennsylvanian (Missourian), Lansing and Kansas City Groups in Eastern Kansas: Kansas Geological Society Guidebook, 41st Annual Field Trip, October 14-15, 1989, Kansas Geological Survey Open-File Report 89-44, 211 p.

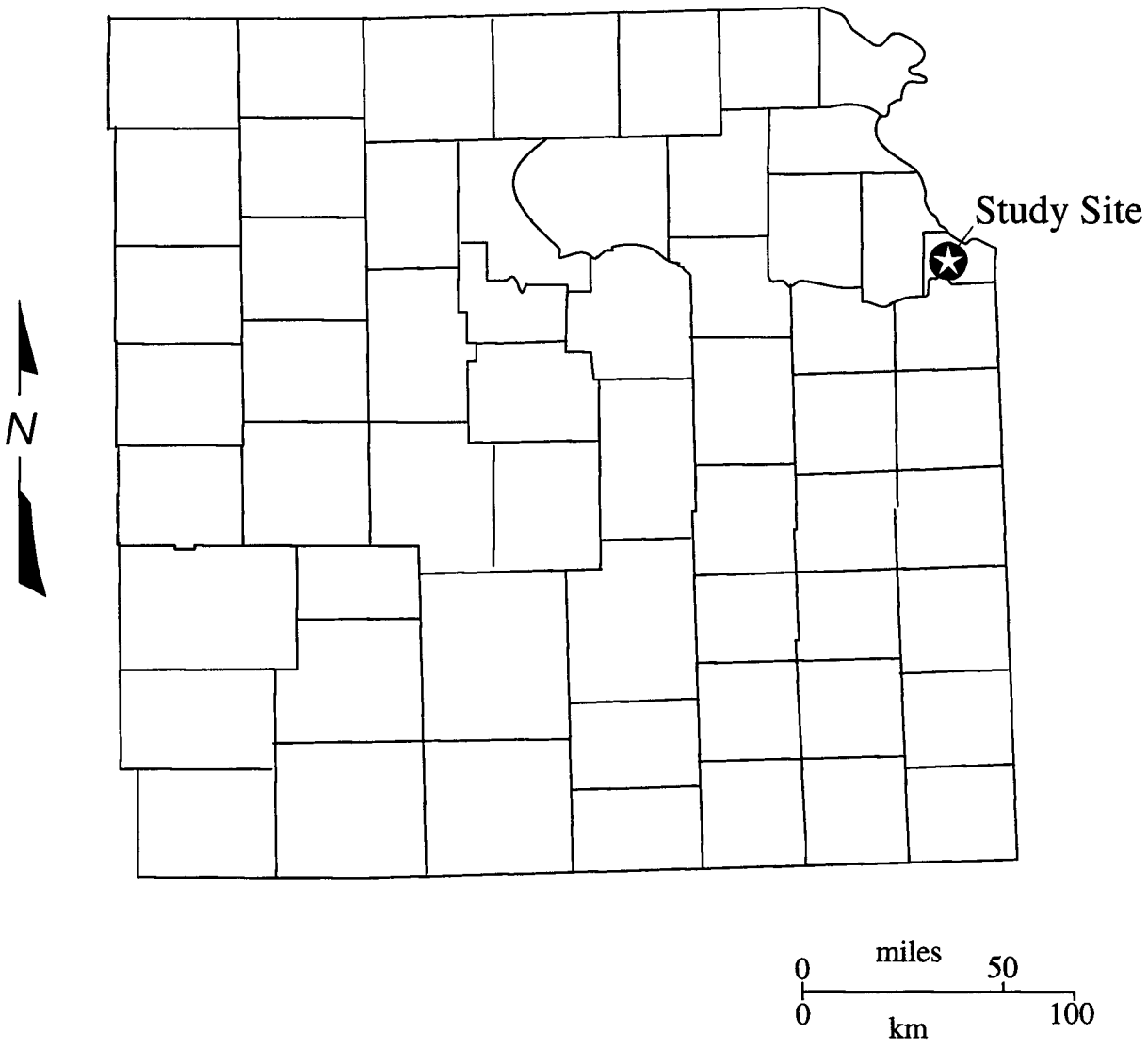

Figure 1. Map showing the location of the study site in Wyandotte County, eastern Kansas.

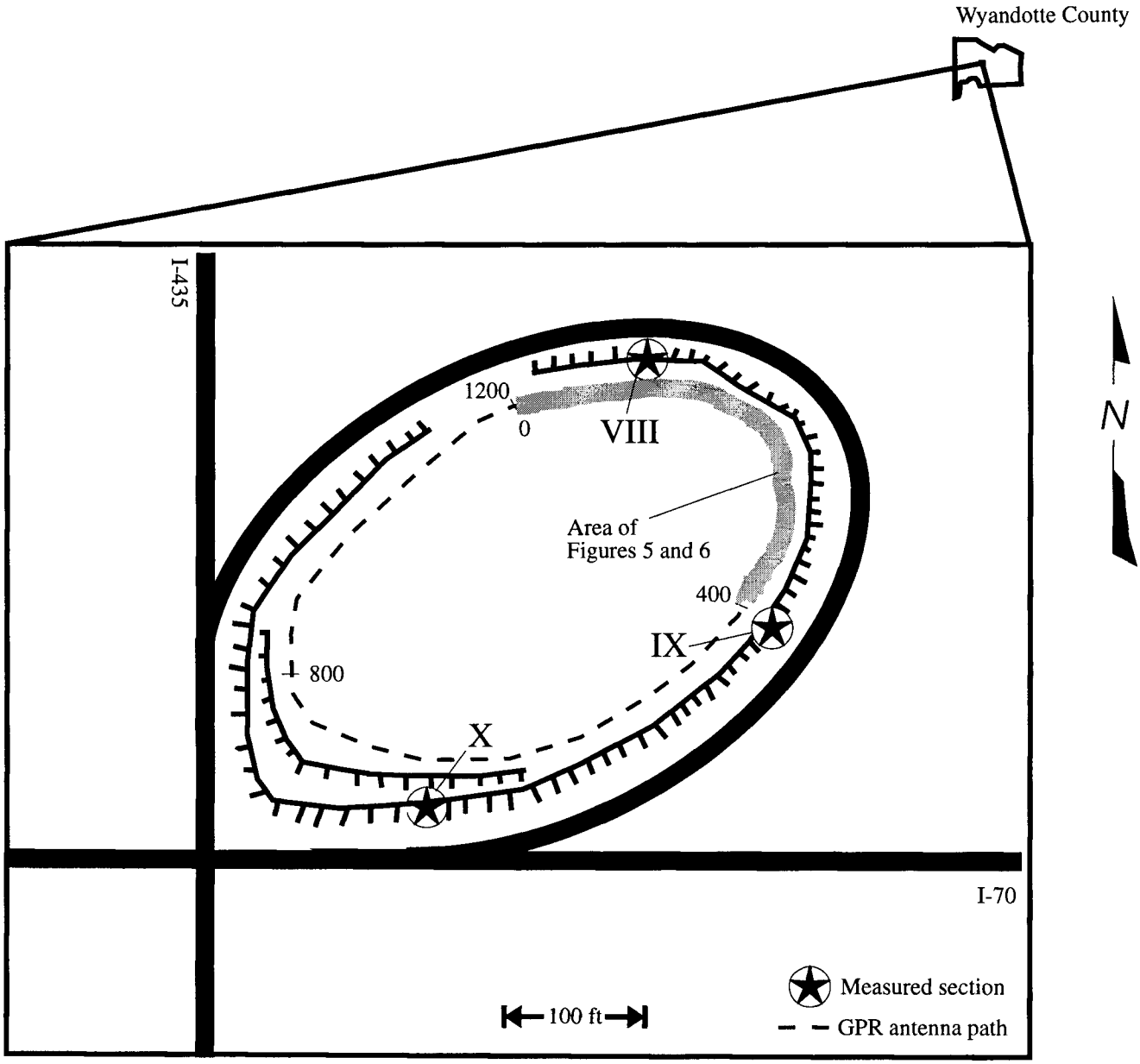

Figure 2. Map of the study site detailing the extent of the outcrop, the GPR profile location, and the data regions shown in Figures 5 and 6. The locations of the measured sections in Figure 3 (VIII, IX, and X) are shown as well.

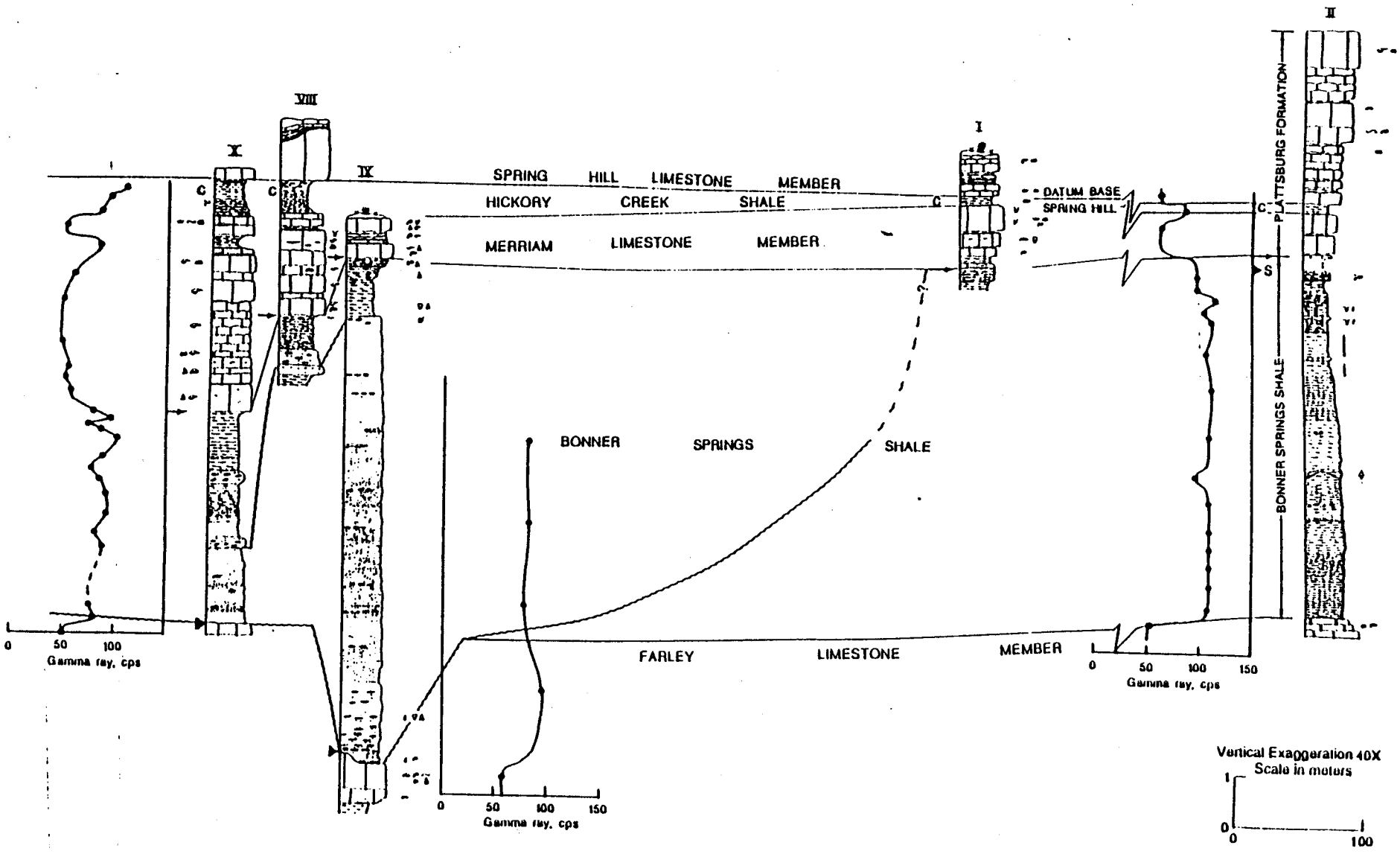

Figure 3. Stratigraphic cross-section from Enos et al. (1989) of the Merriam Limestone Member and Bonner Springs Shale. The locations of measured sections VIII, IX, and X are shown in Figure 2.

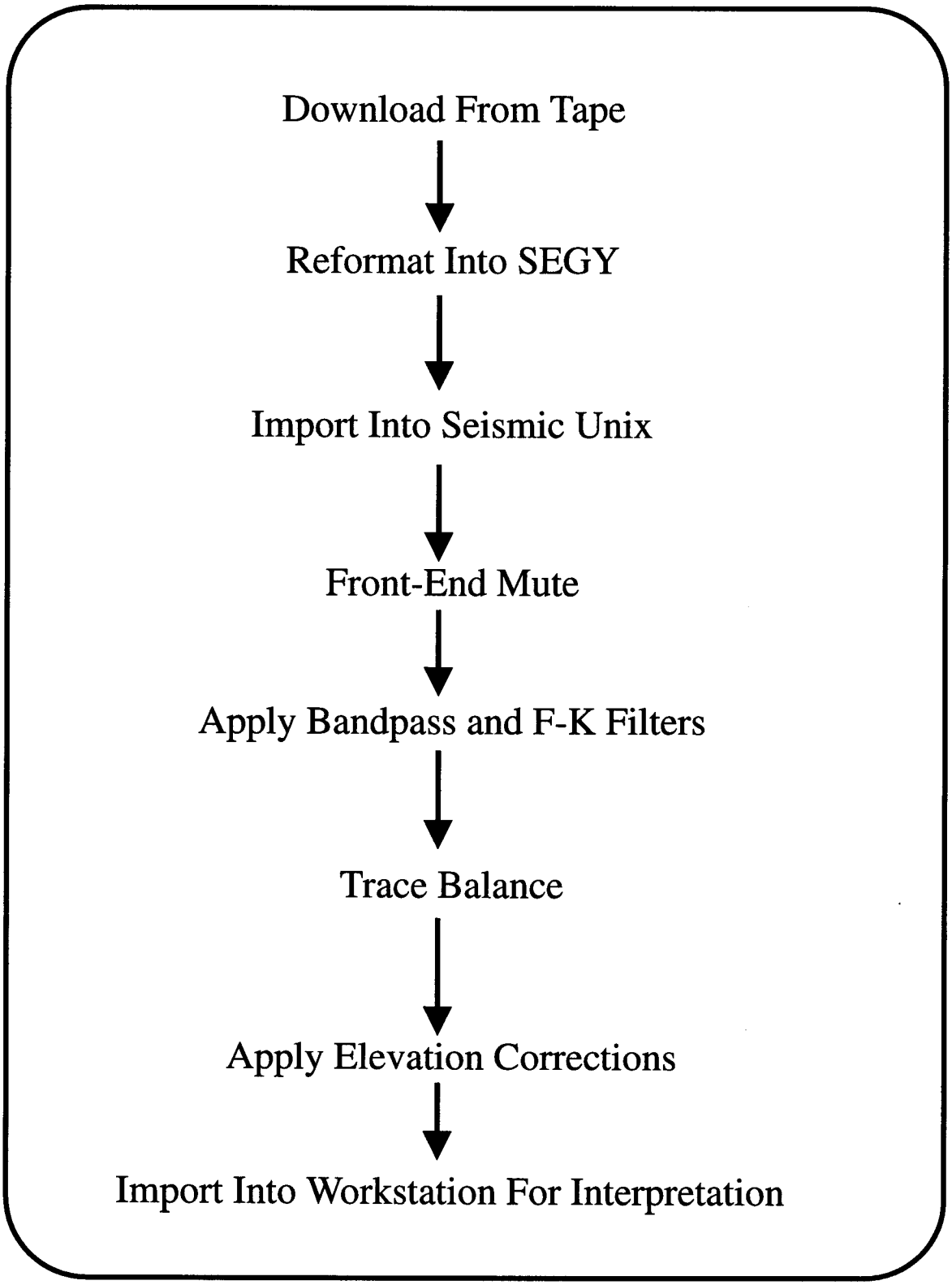

Figure 4. A generalized ground-penetrating radar data processing flow chart. Note that the steps taken are very similar to conventional post-stack seismic data processing.

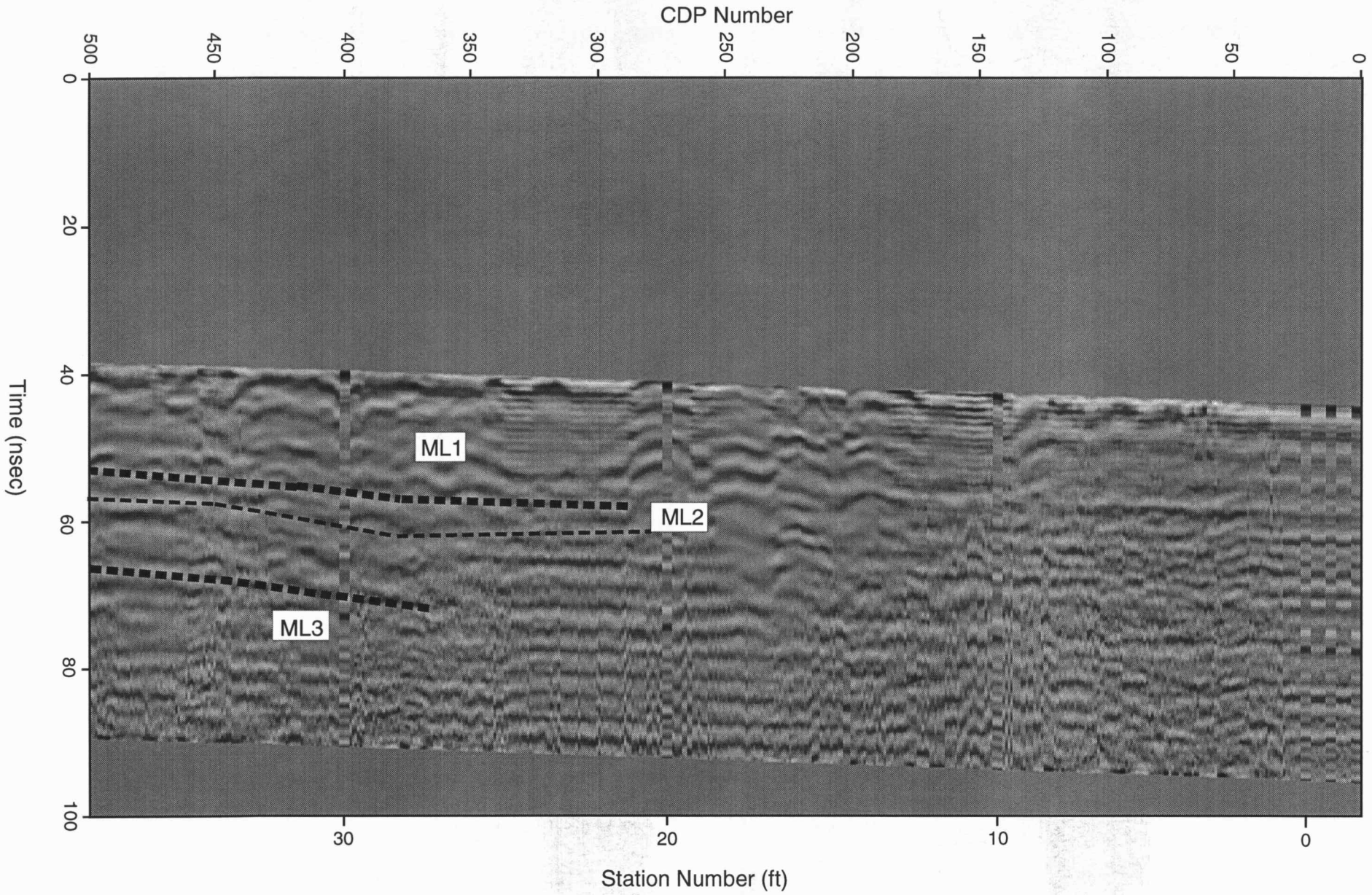

Figure 5a. GPR profile from the I-70/I-435 interchange.

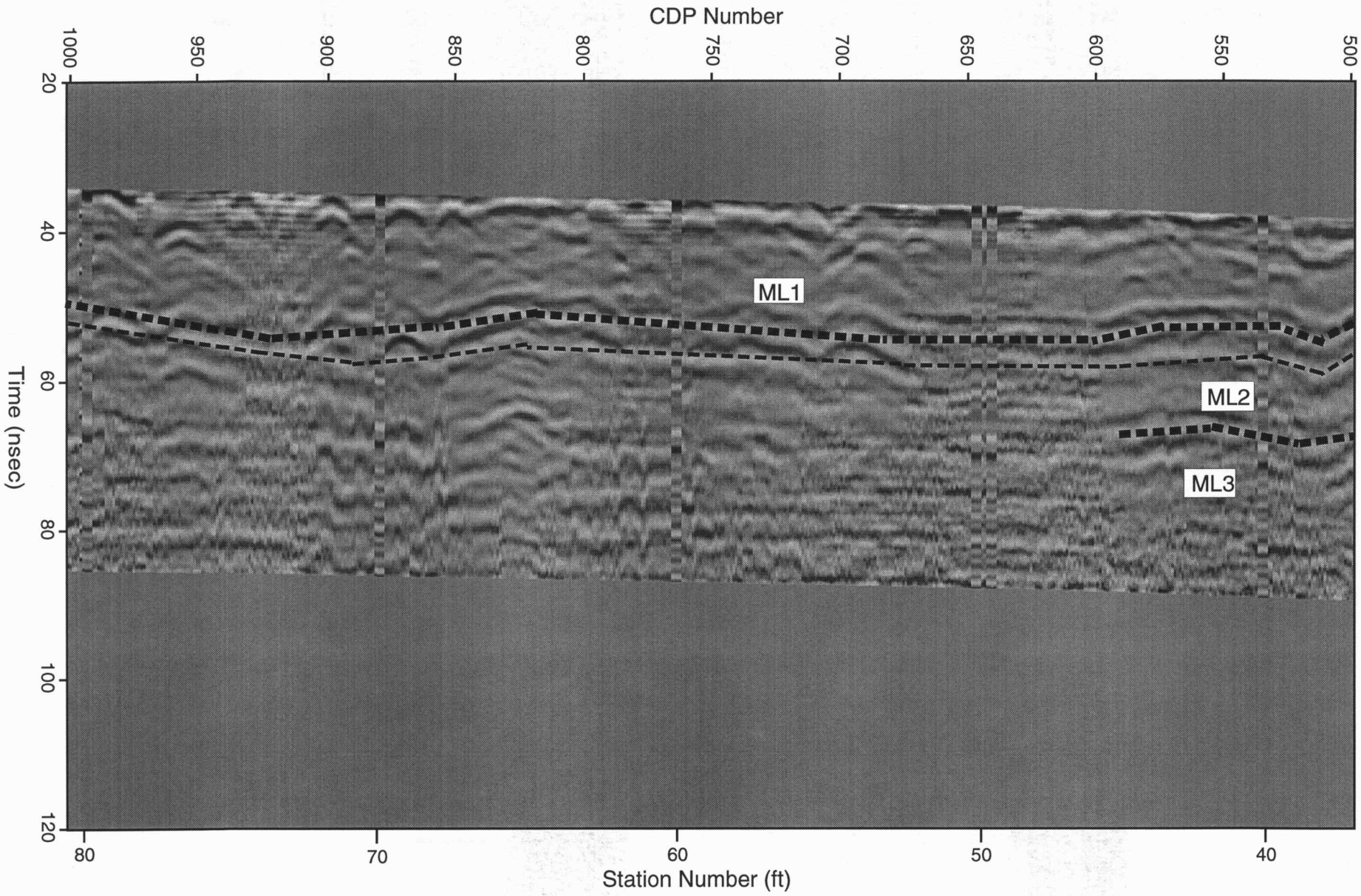

Figure 5b. Continuation of GPR profile from the I-70/I-435 interchange.

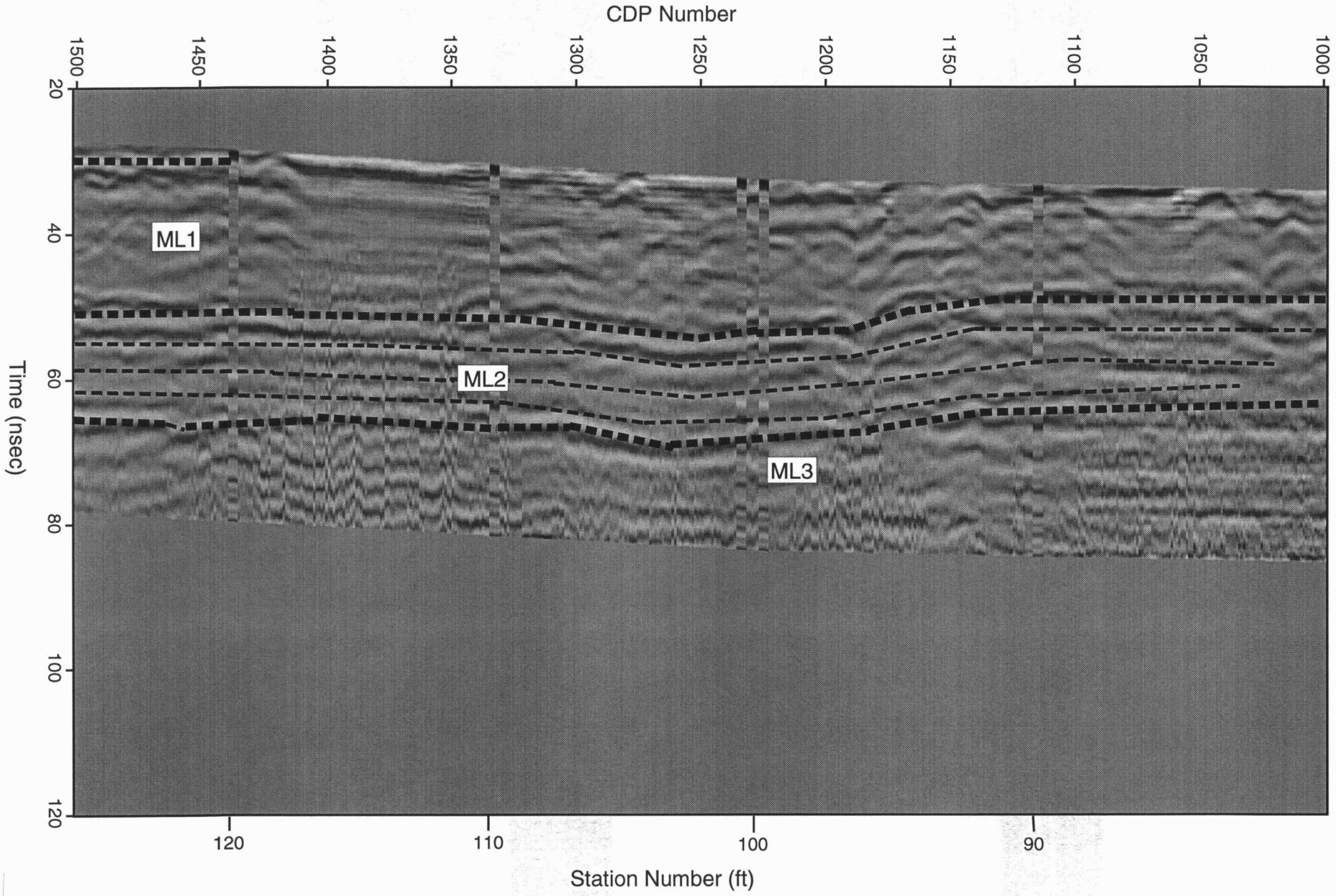

Figure 5c. Continuation of GPR profile from the I-70/I-435 interchange.

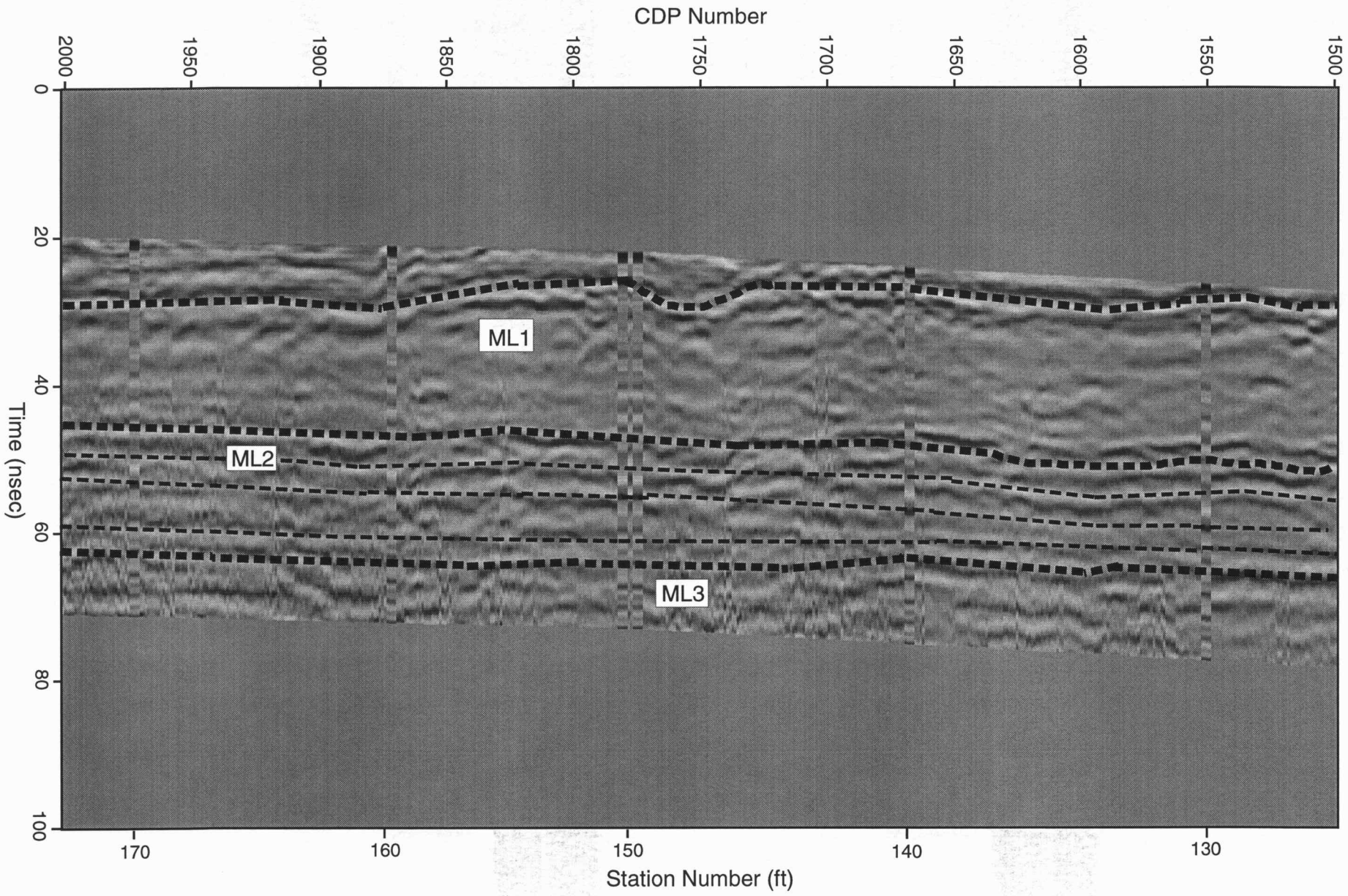

Figure 5d. Continuation of GPR profile from the I-70/I-435 interchange.

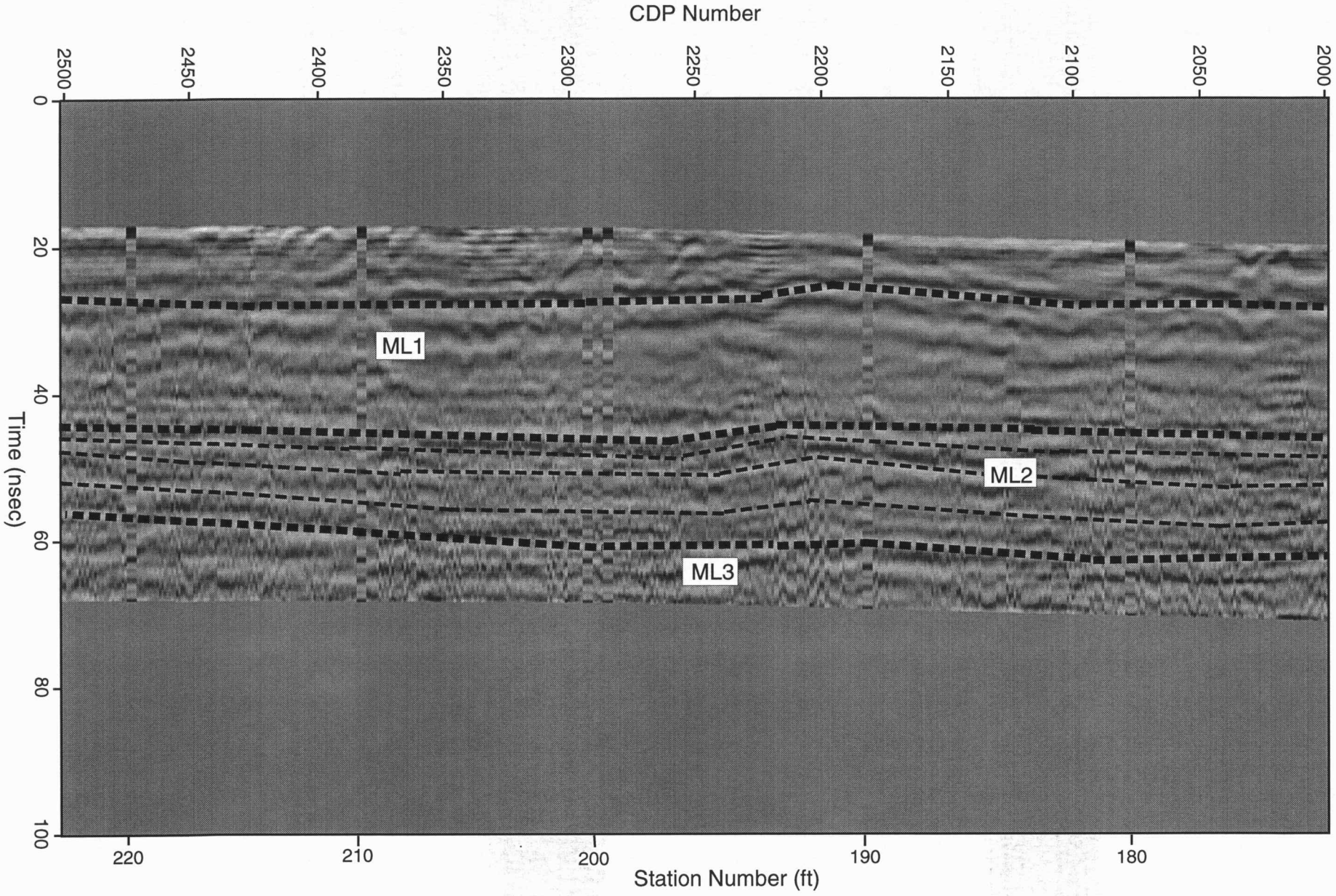

Figure 5e. Continuation of GPR profile from the I-70/I-435 interchange.

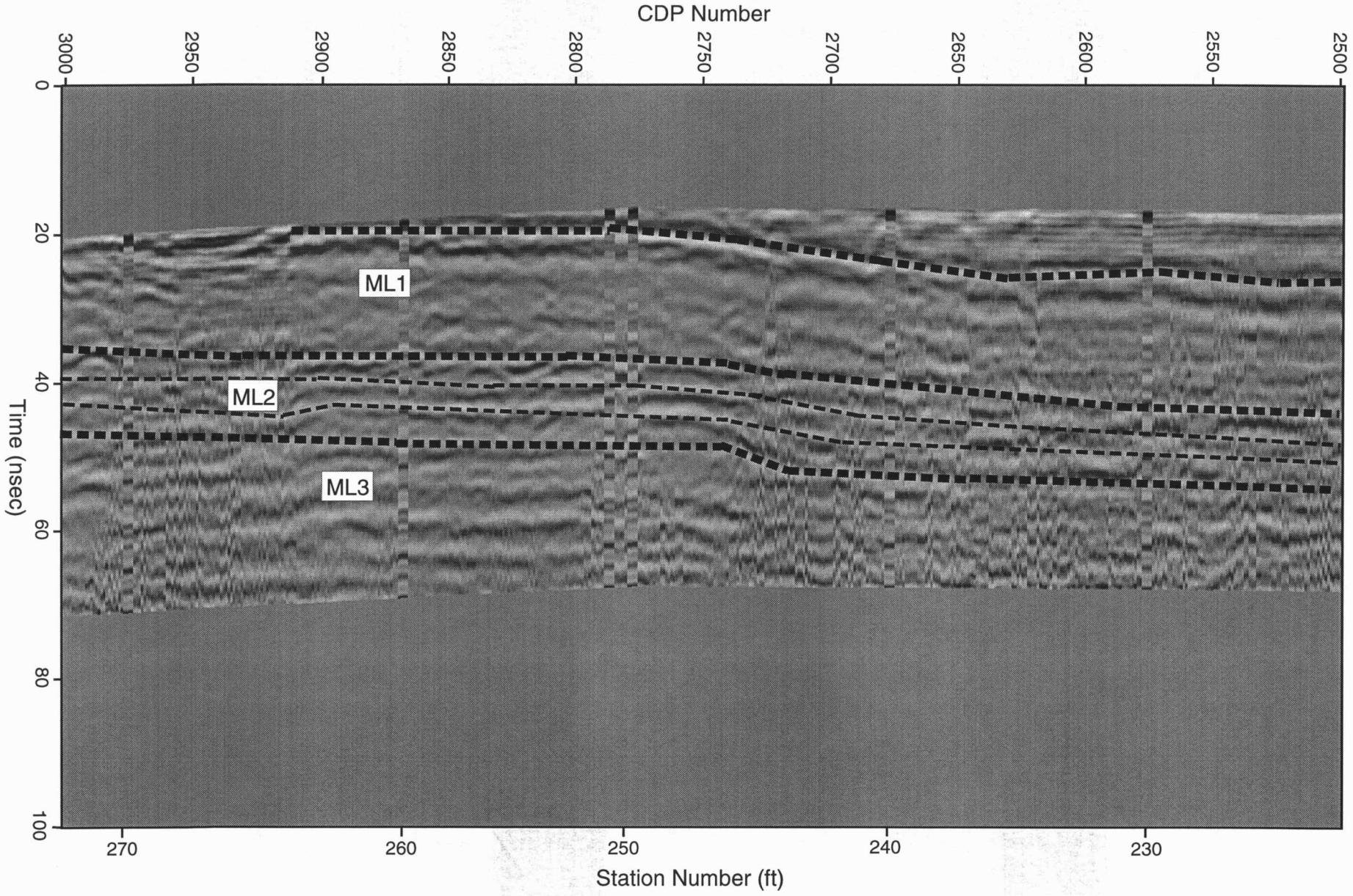

Figure 5f. Continuation of GPR profile from the I-70/I-435 interchange.

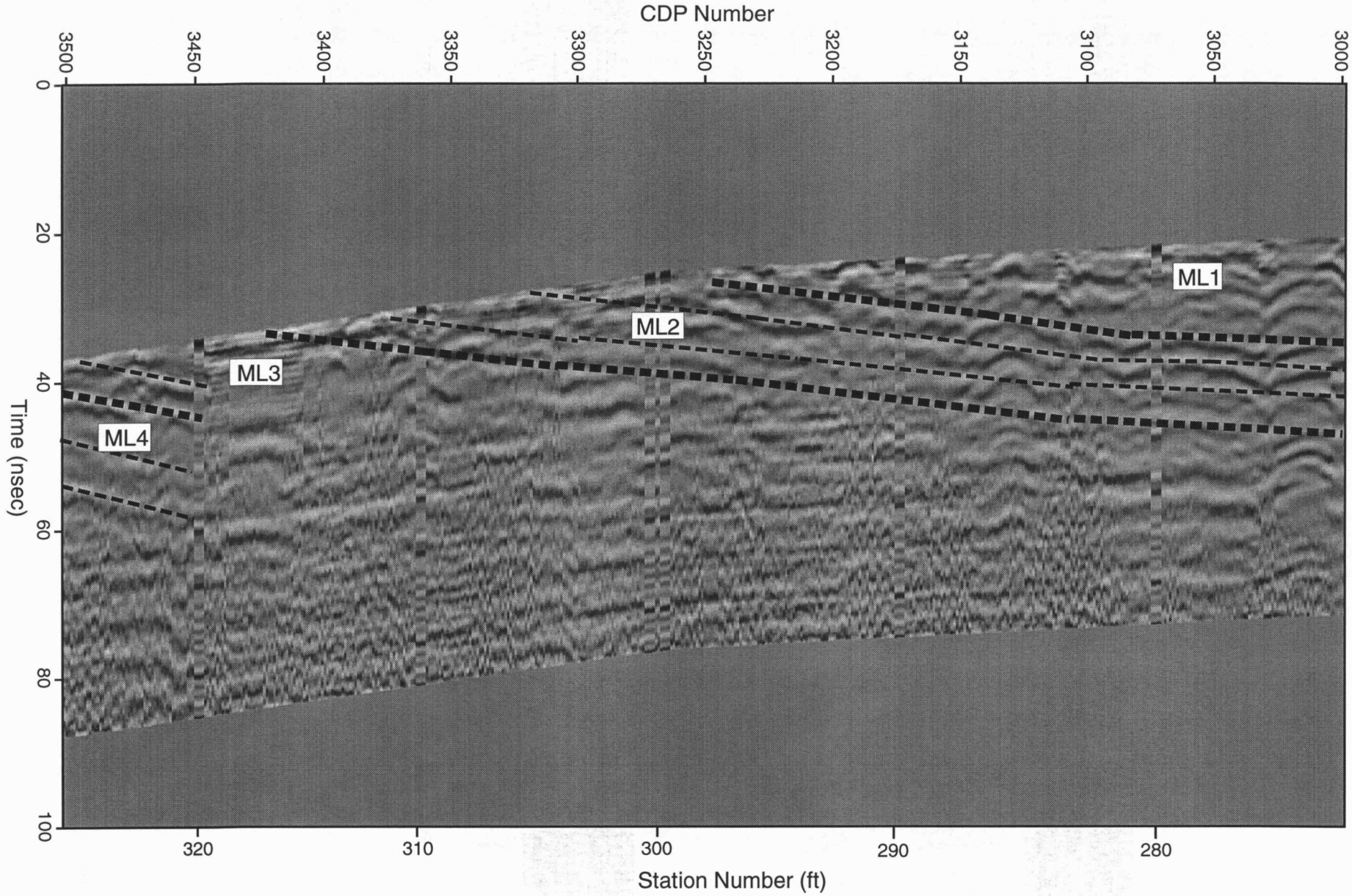

Figure 5g. Continuation of GPR profile from the I-70/I-435 interchange.

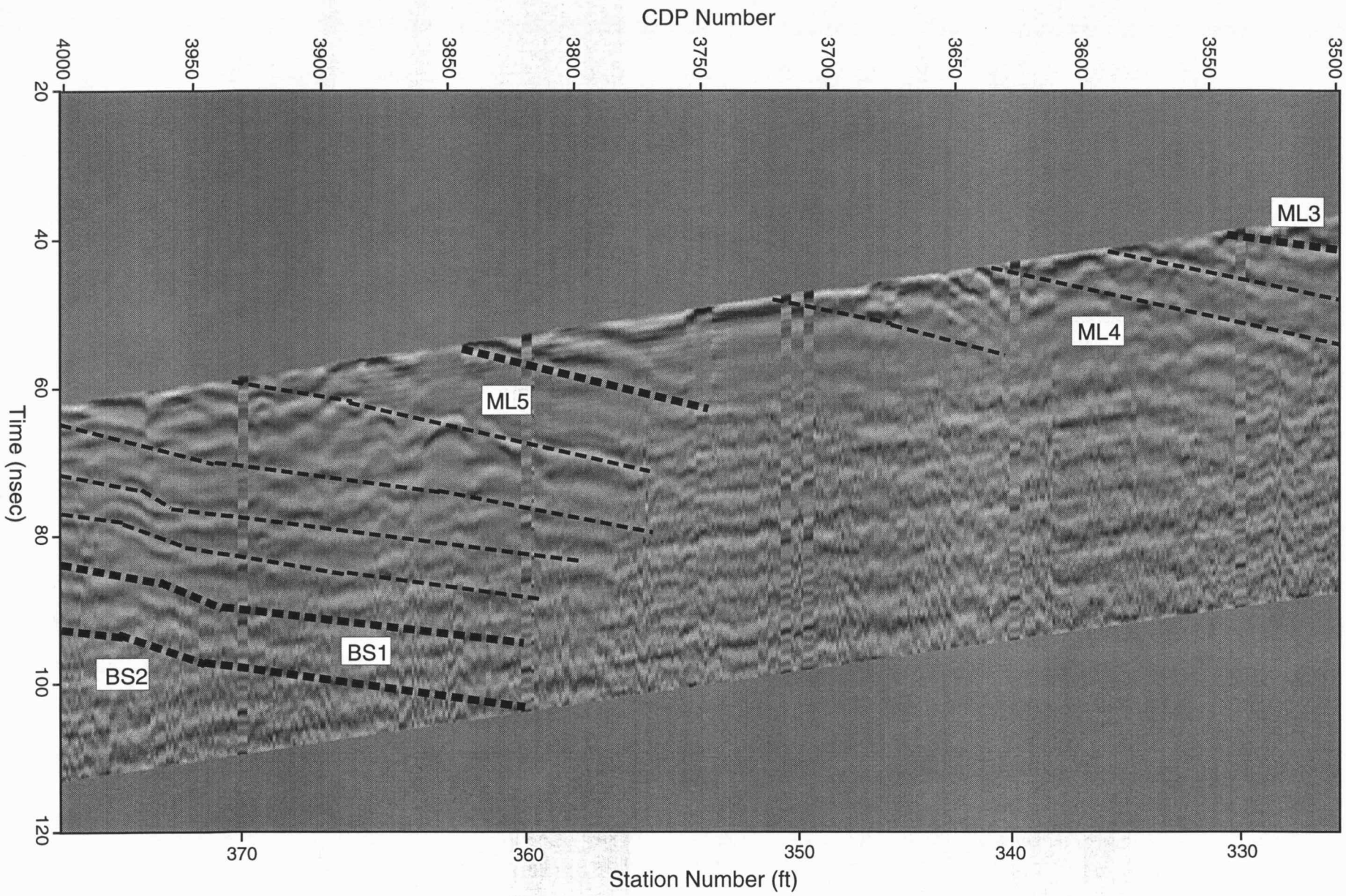

Figure 5h. Continuation of GPR profile from the I-70/I-435 interchange.

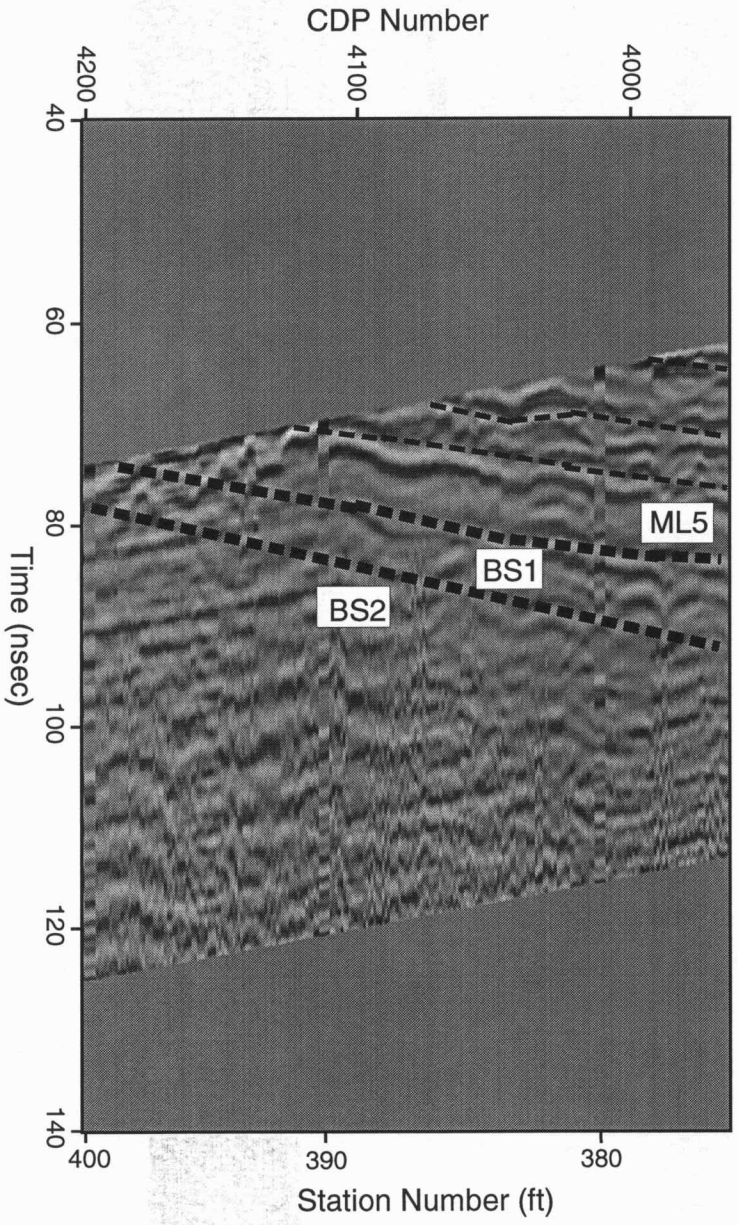

Figure 5i. Continuation of GPR profile from the I-70/I-435 interchange.

Figure 6a. Photograph of GPR stations 0-50.

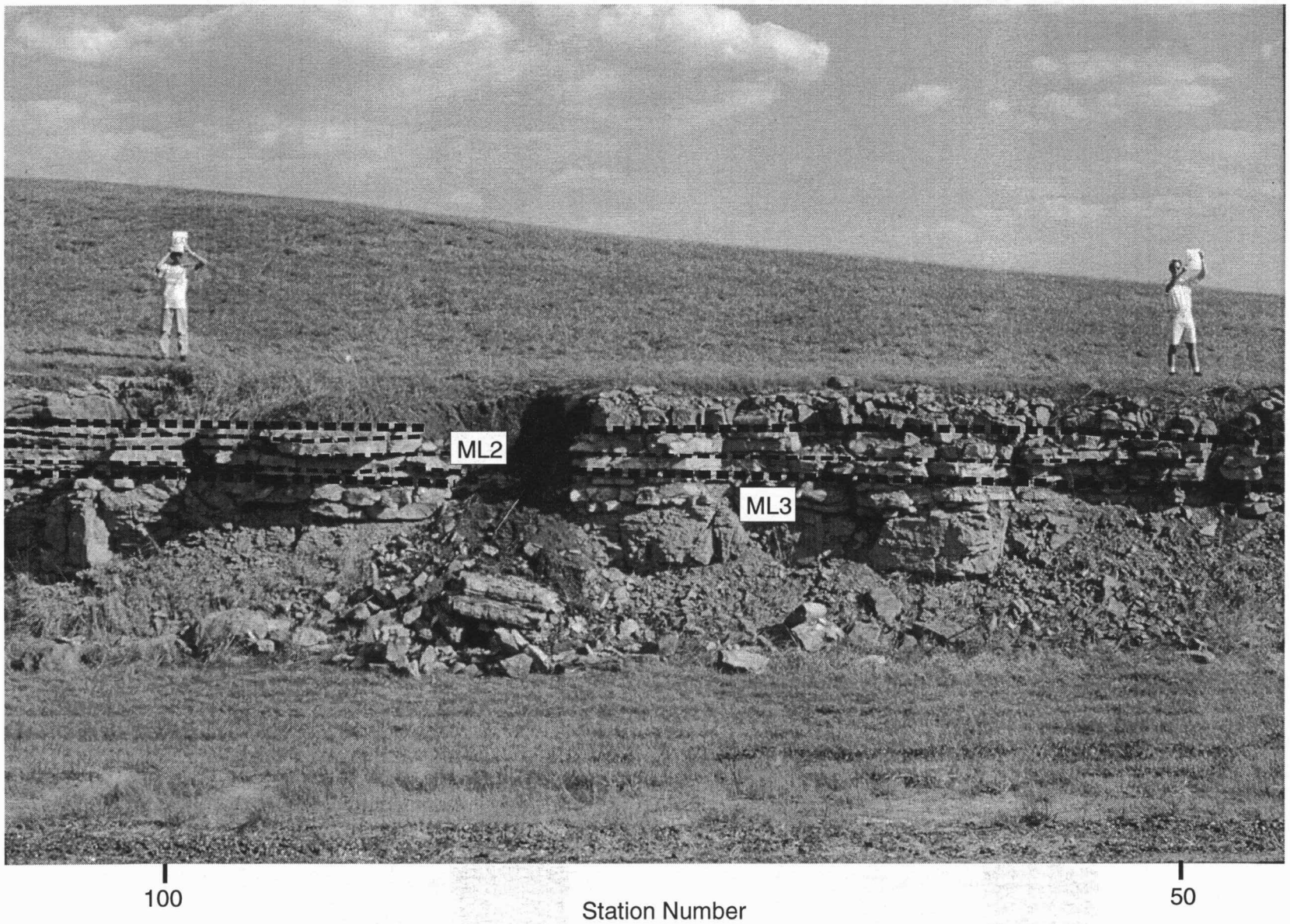

Figure 6b. Photograph of GPR Stations 50-100.

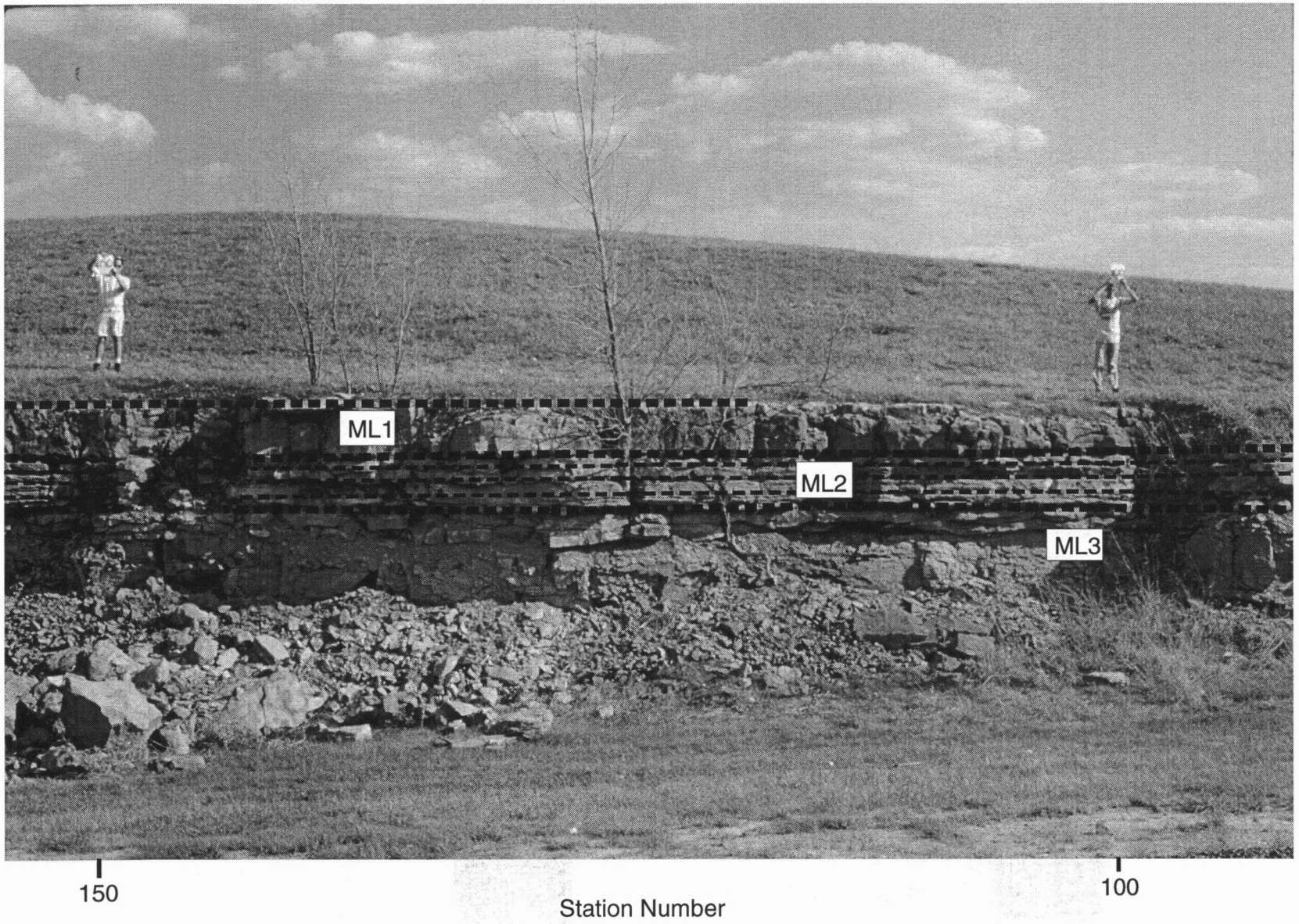

Figure 6c. Photograph of GPR Stations 100-150.

Figure 6d. Photograph of GPR Stations 150-200.

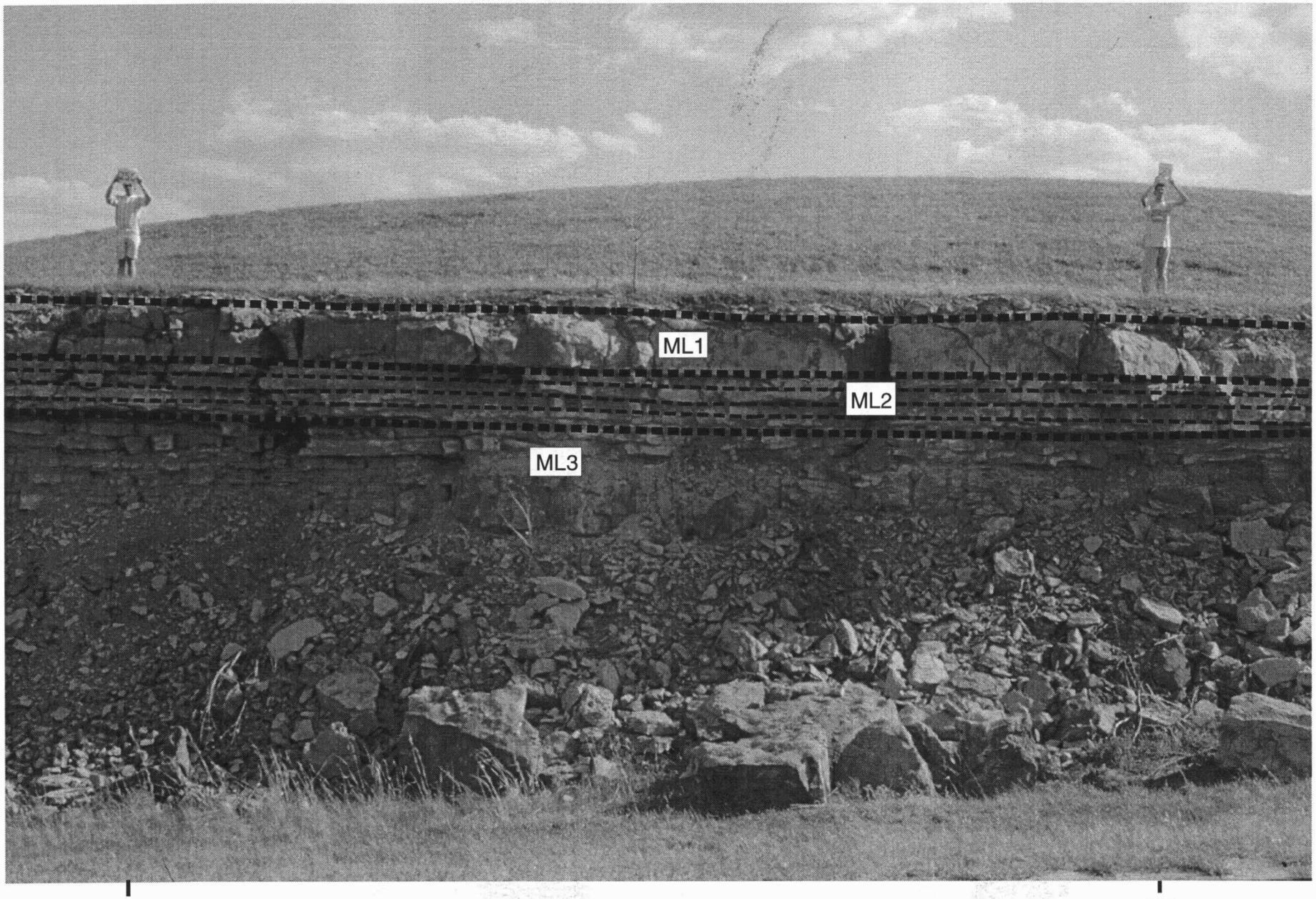

Figure 6e. Photograph of GPR Stations 200-250.

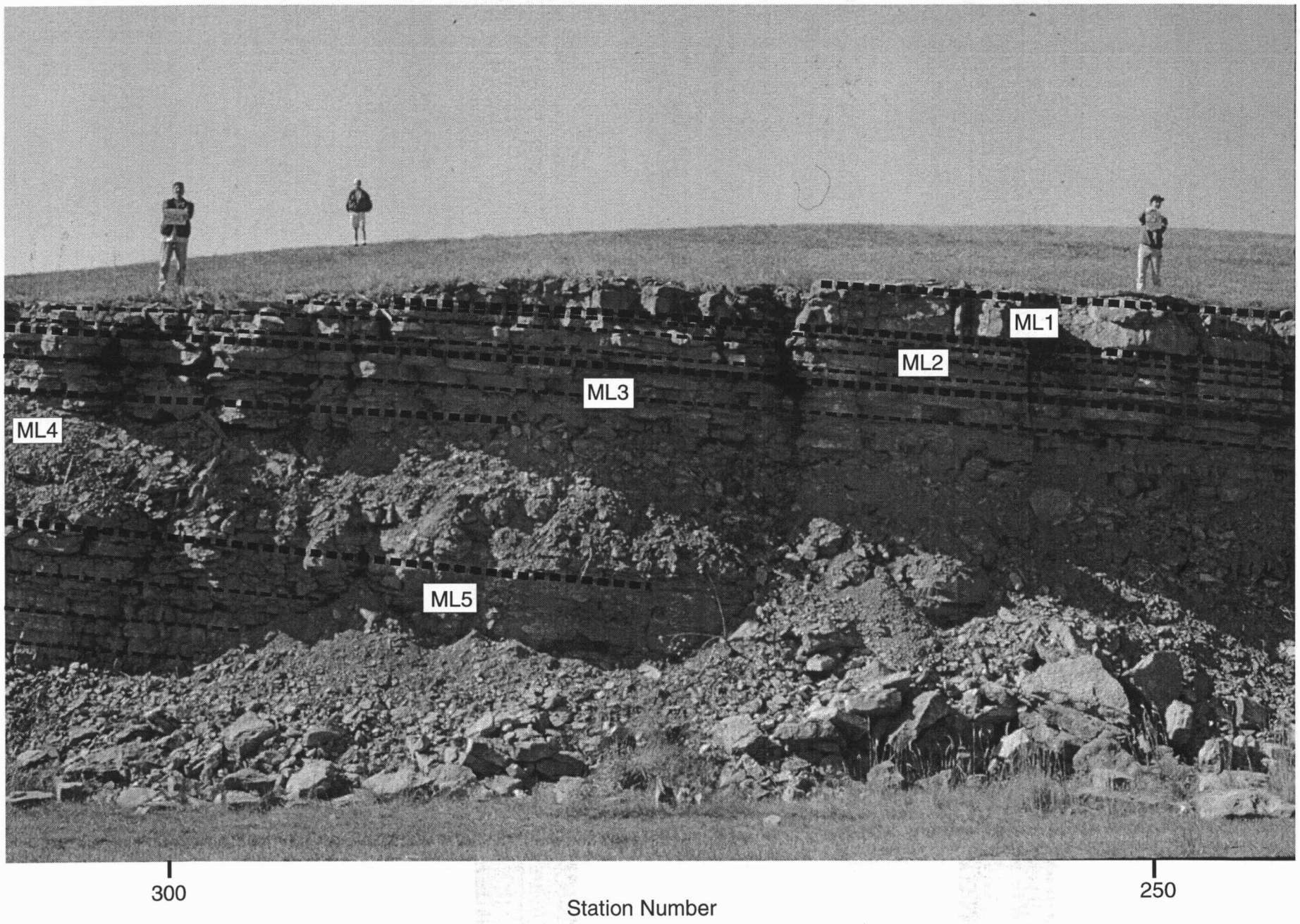

Figure 6f. Photograph of GPR Stations 250-300.

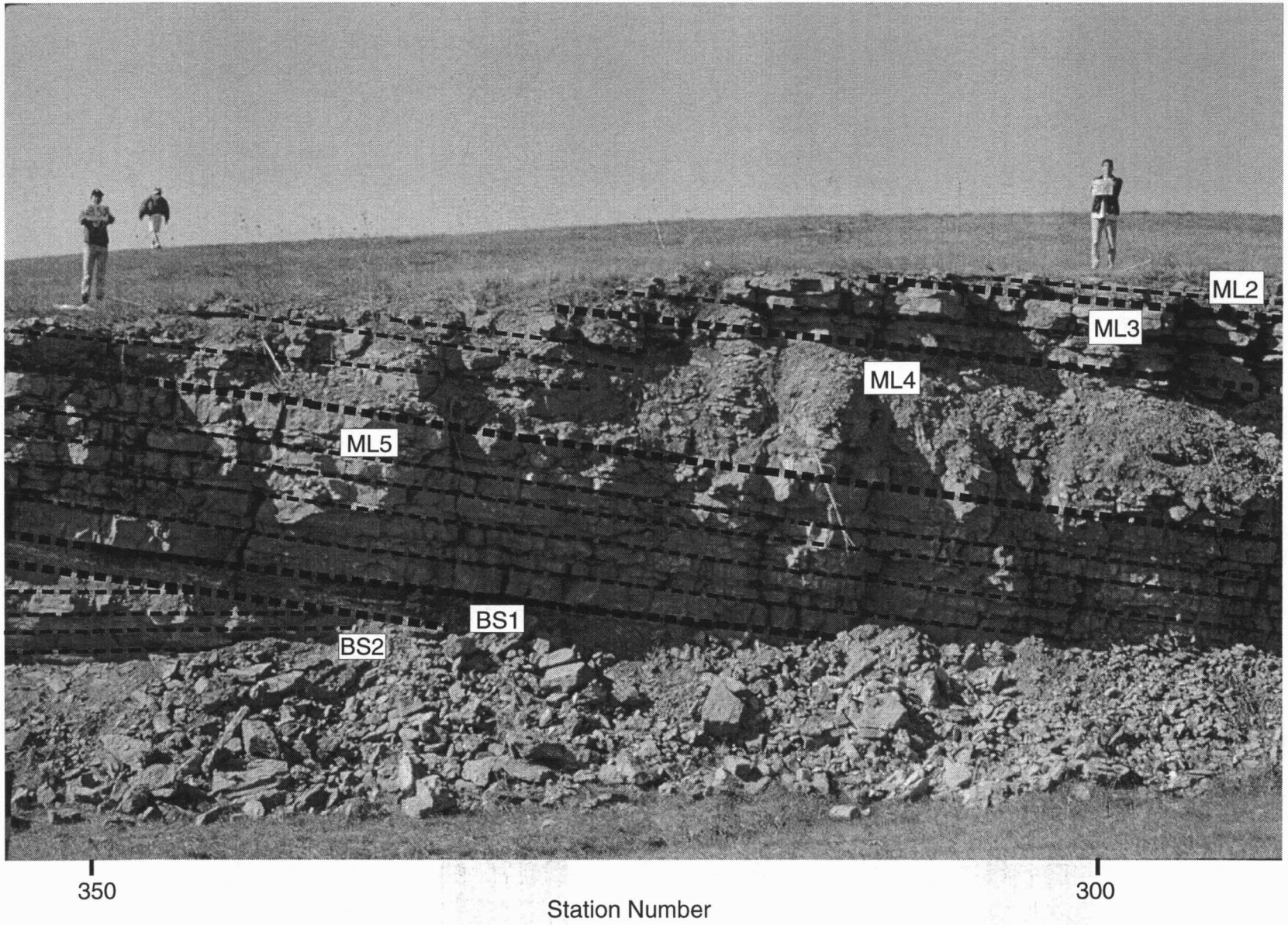

Figure 6g. Photograph of GPR Stations 300-350.

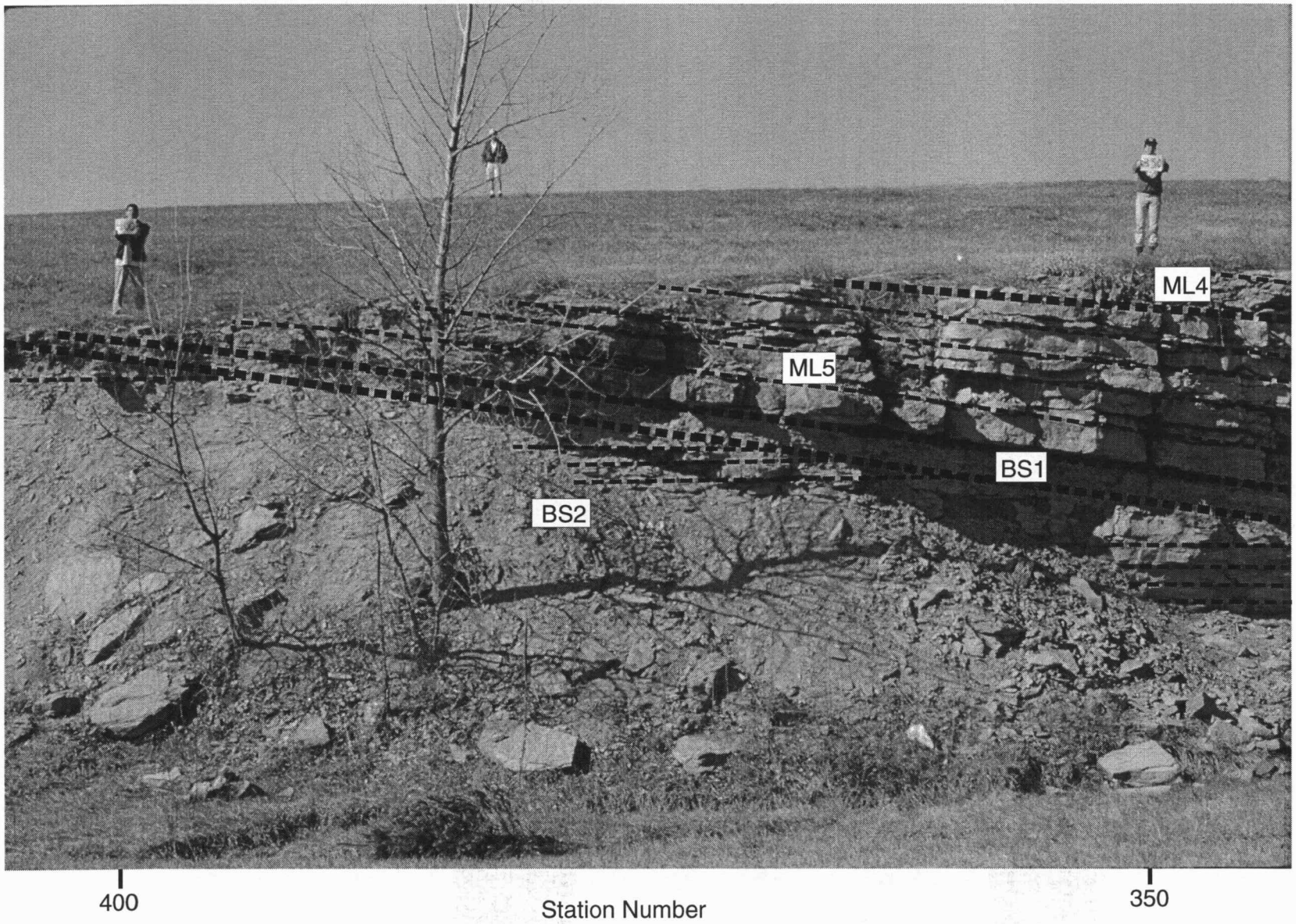

Figure 6h. Photograph of GPR Stations 350-400.

APPENDIX A: UNINTERPRETED DATA

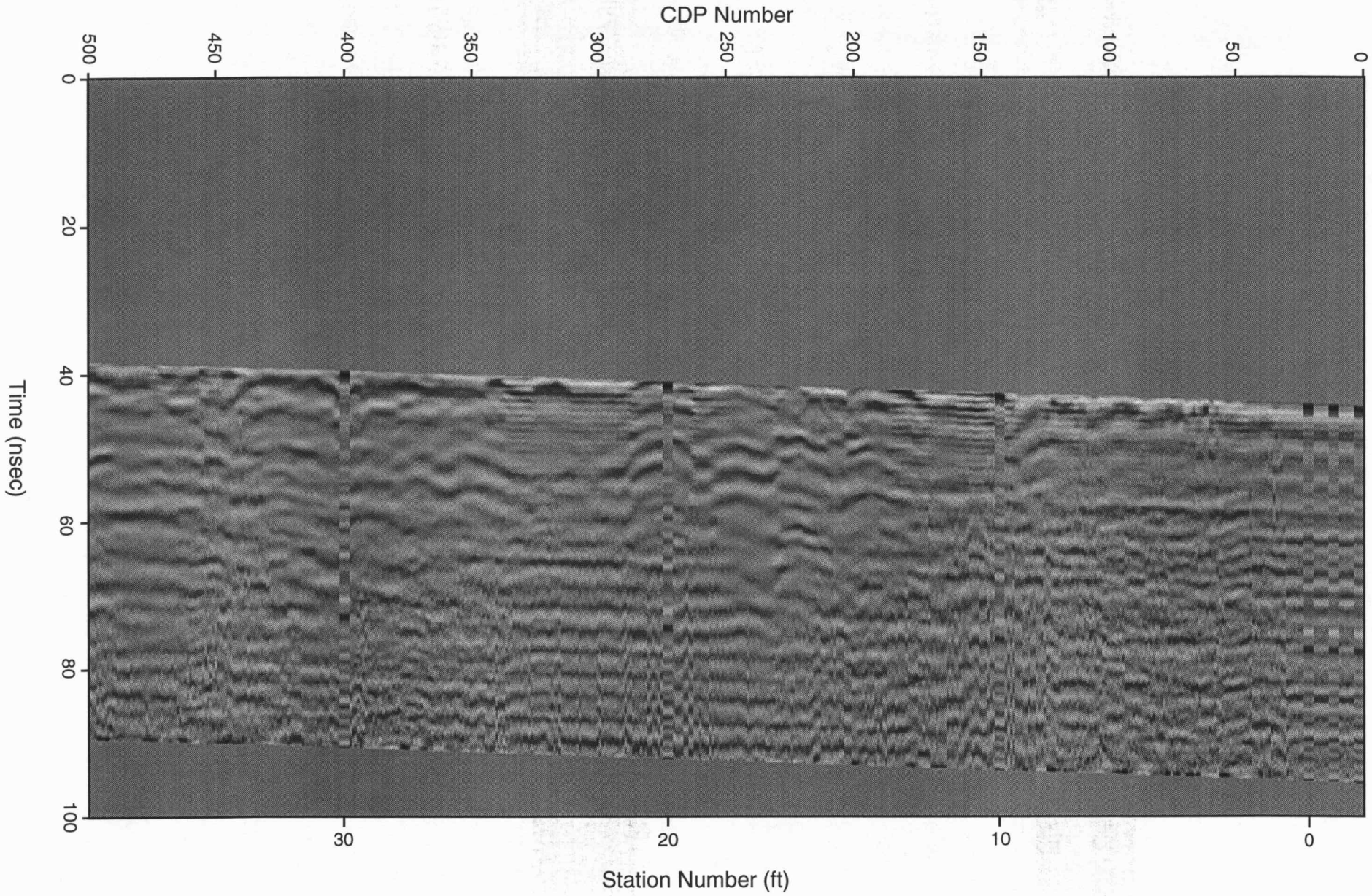

Figure 5a. GPR profile from the I-70/I-435 interchange.

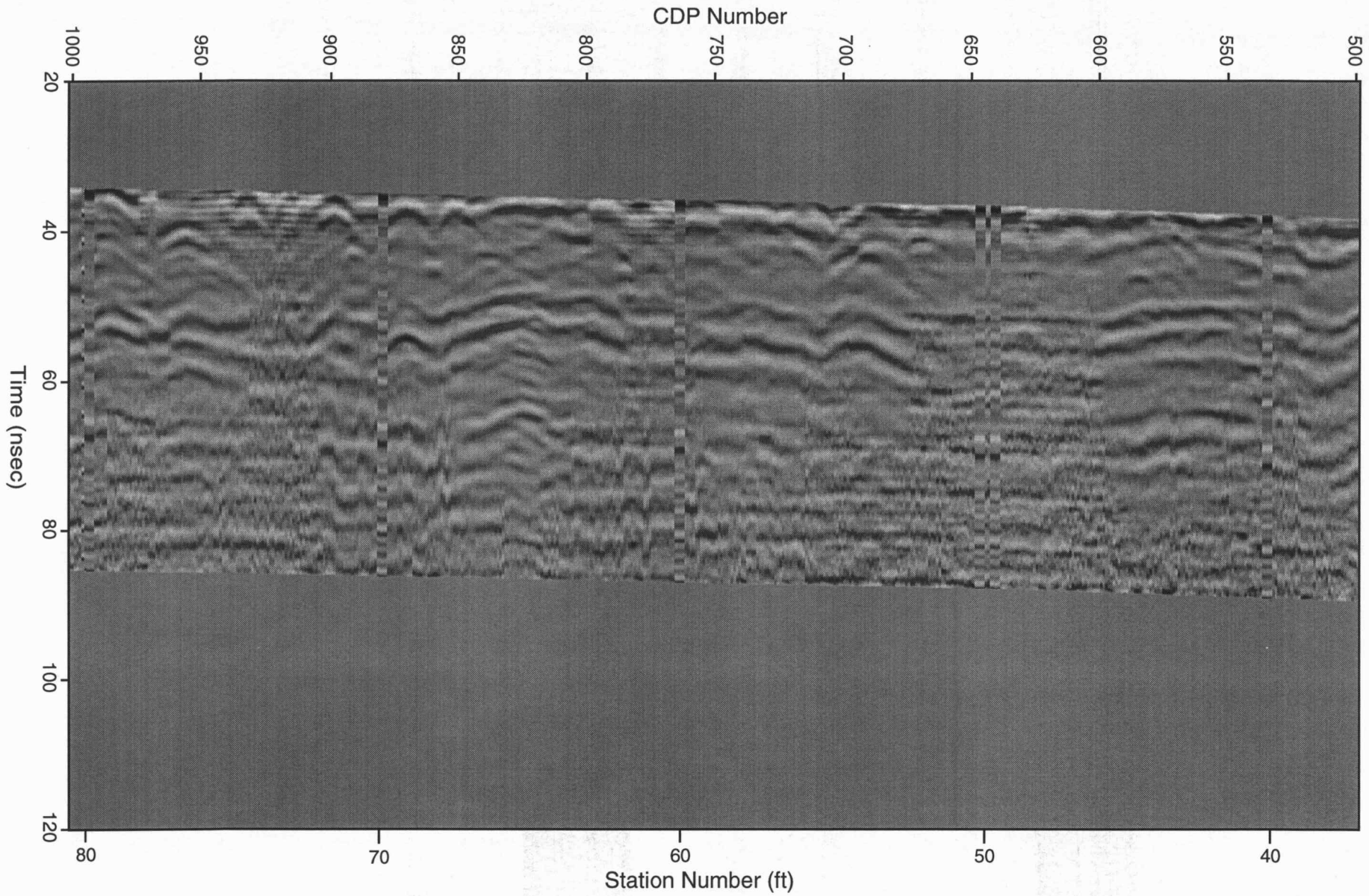

Figure 5b. Continuation of GPR profile from the I-70/I-435 interchange.

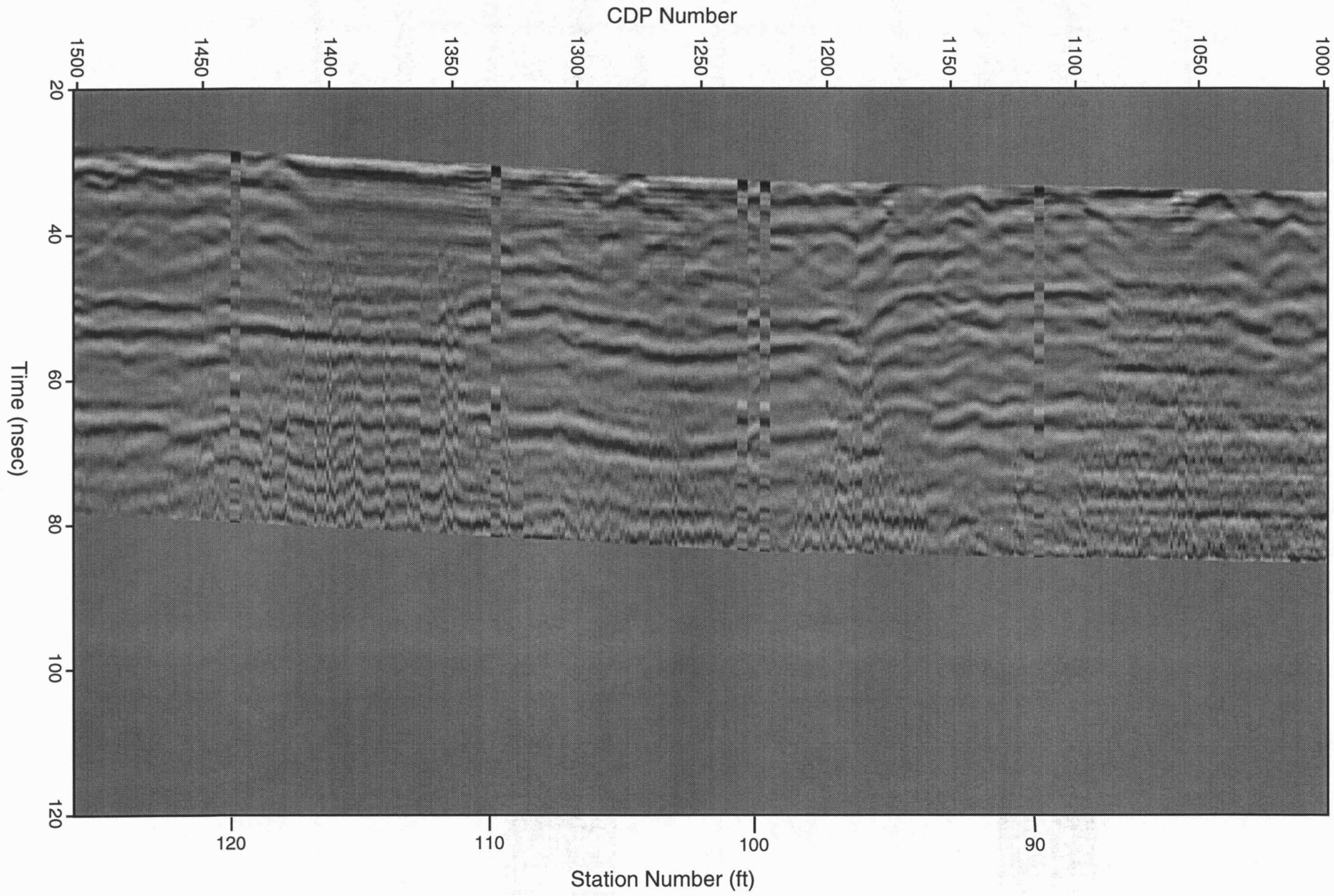

Figure 5c. Continuation of GPR profile from the I-70/I-435 interchange.

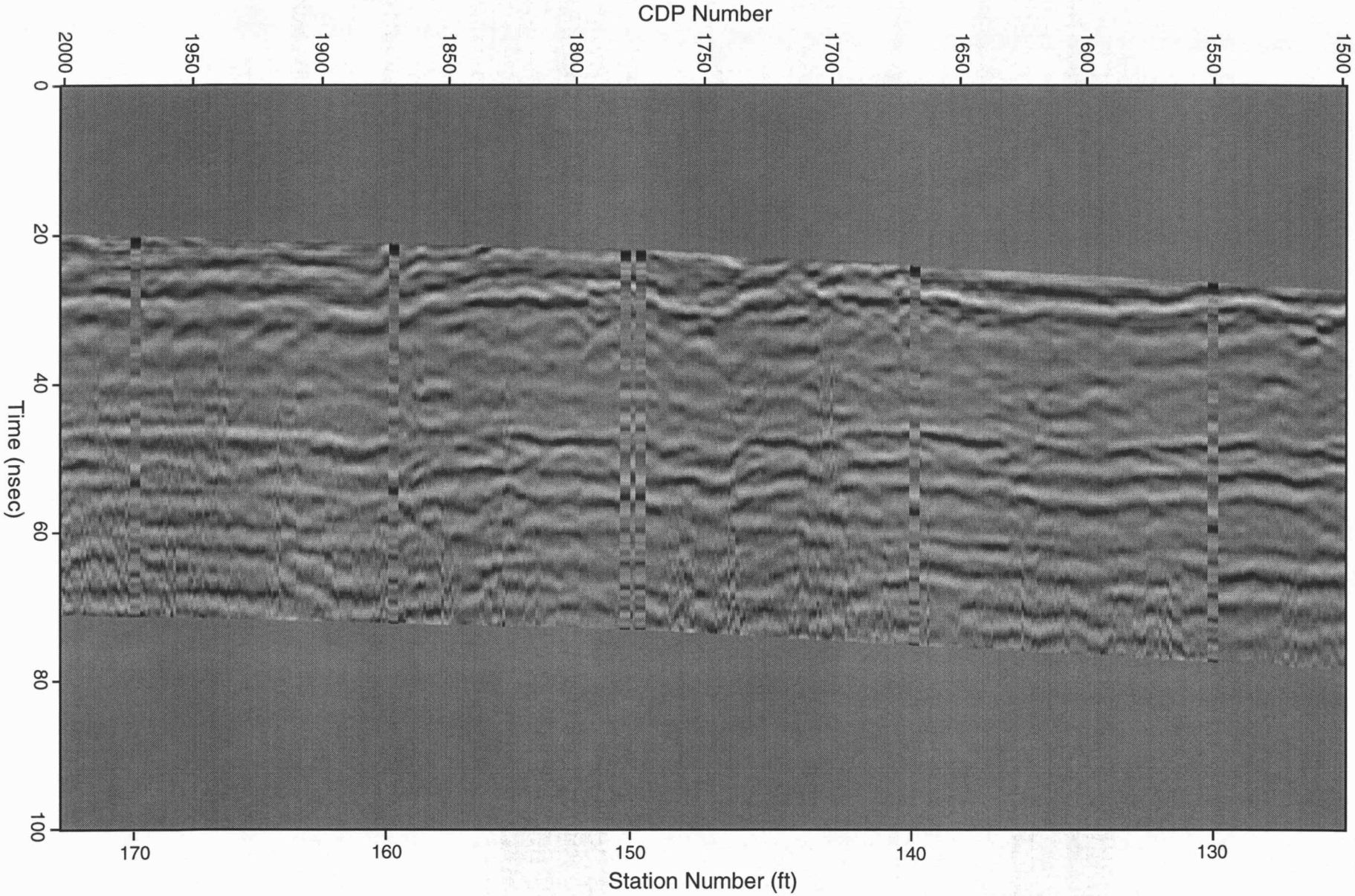

Figure 5d. Continuation of GPR profile from the I-70/I-435 interchange.

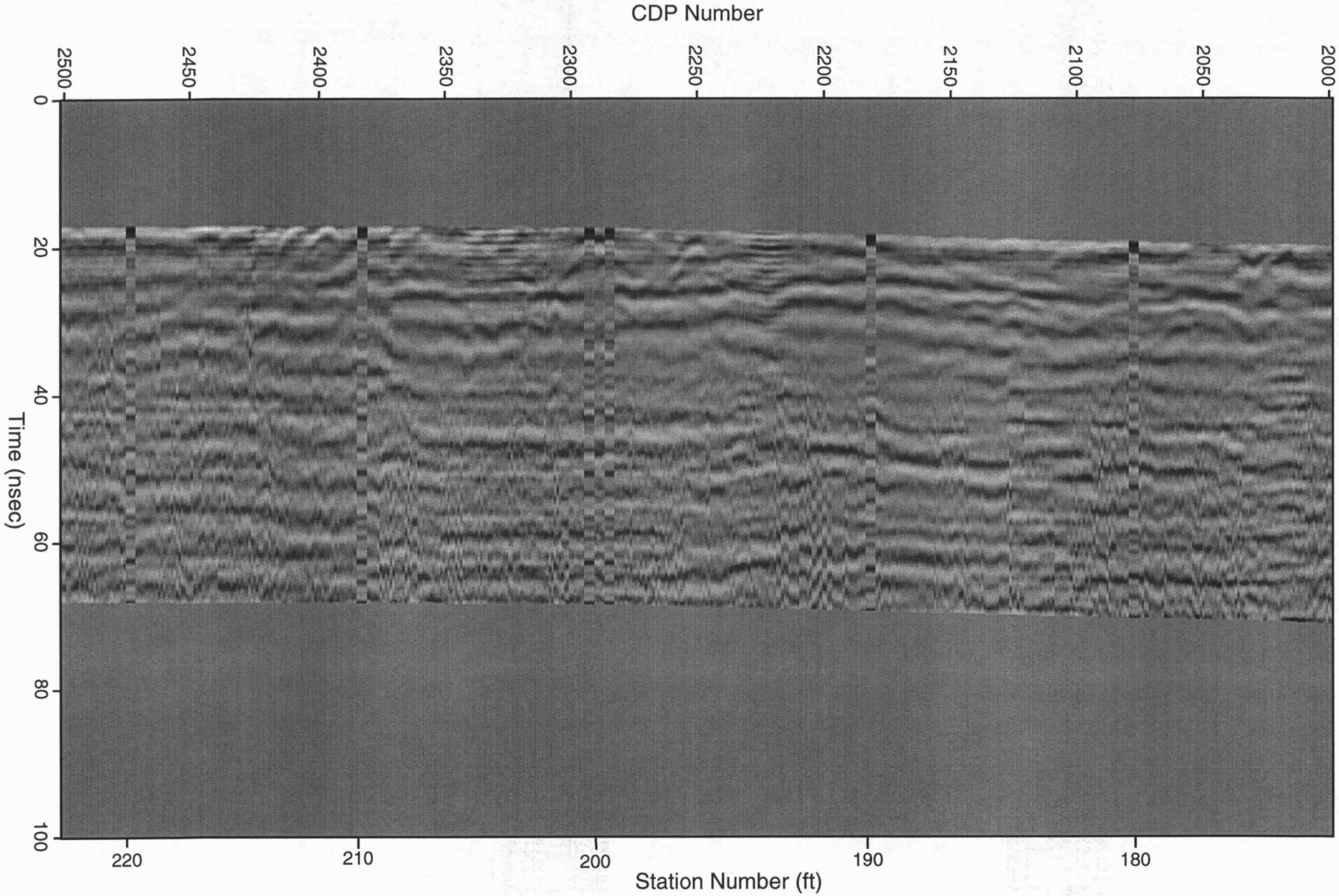

Figure 5e. Continuation of GPR profile from the I-70/I-435 interchange.

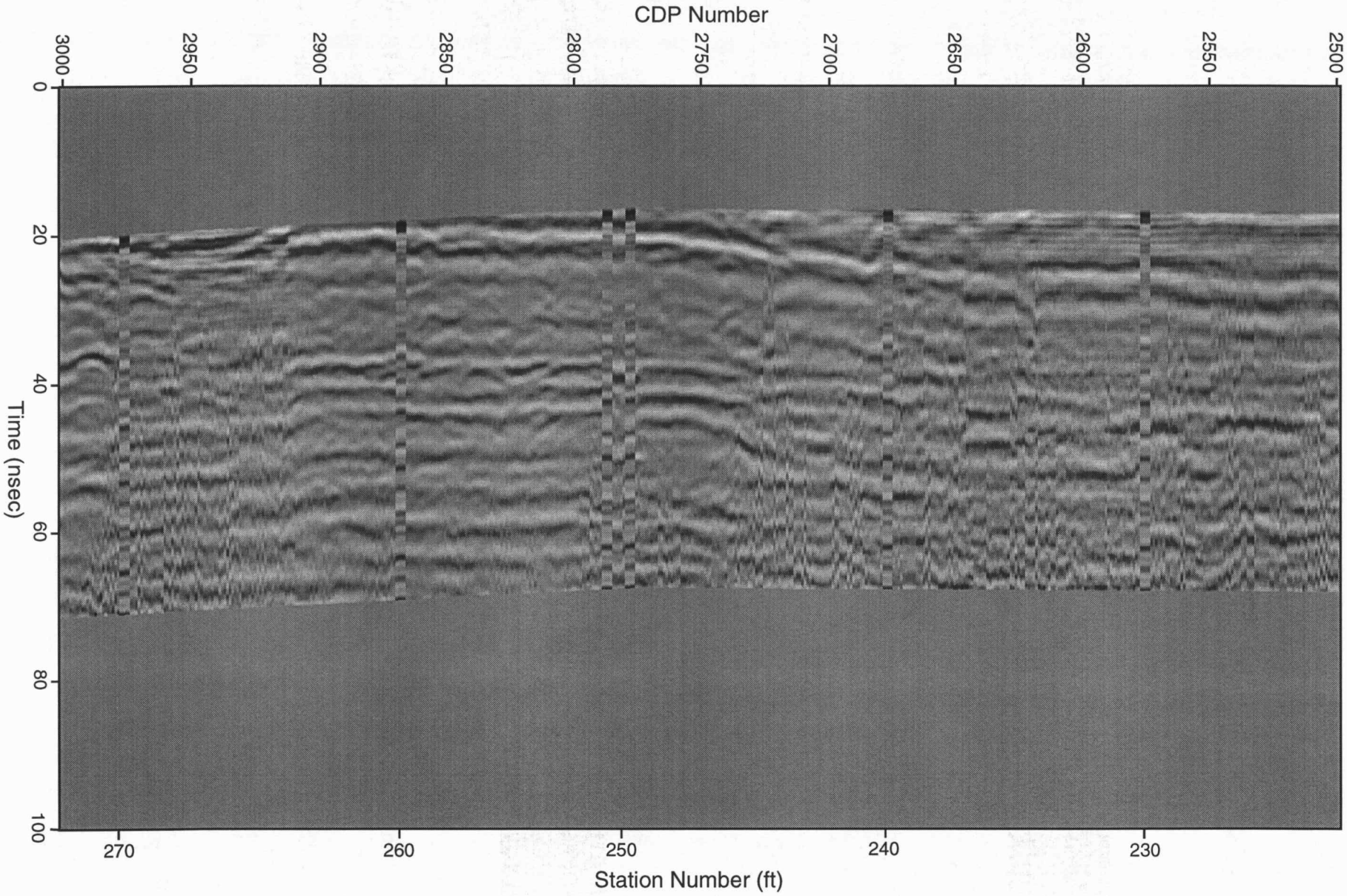

Figure 5f. Continuation of GPR profile from the I-70/I-435 interchange.

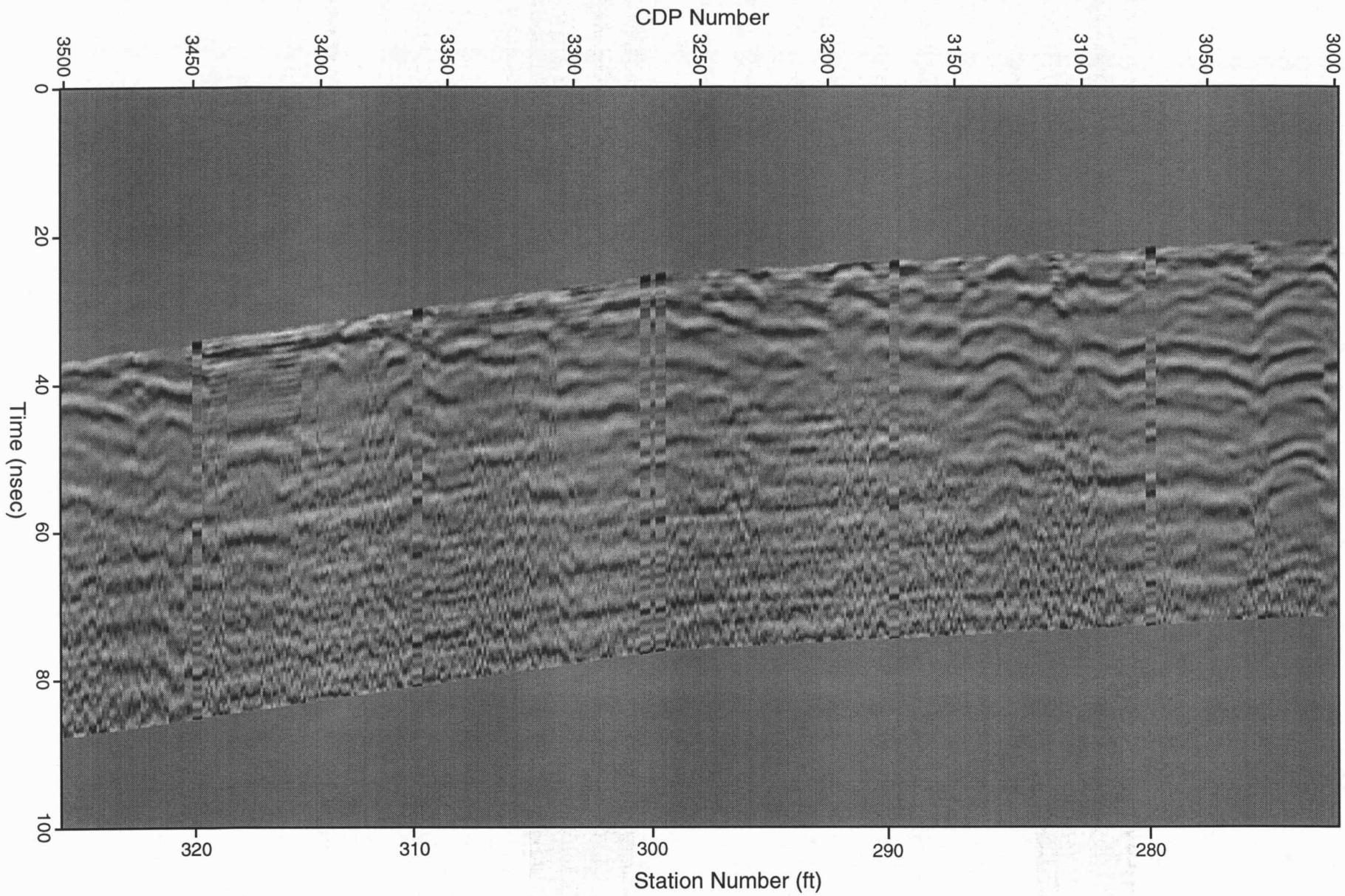

Figure 5g. Continuation of GPR profile from the I-70/I-435 interchange.

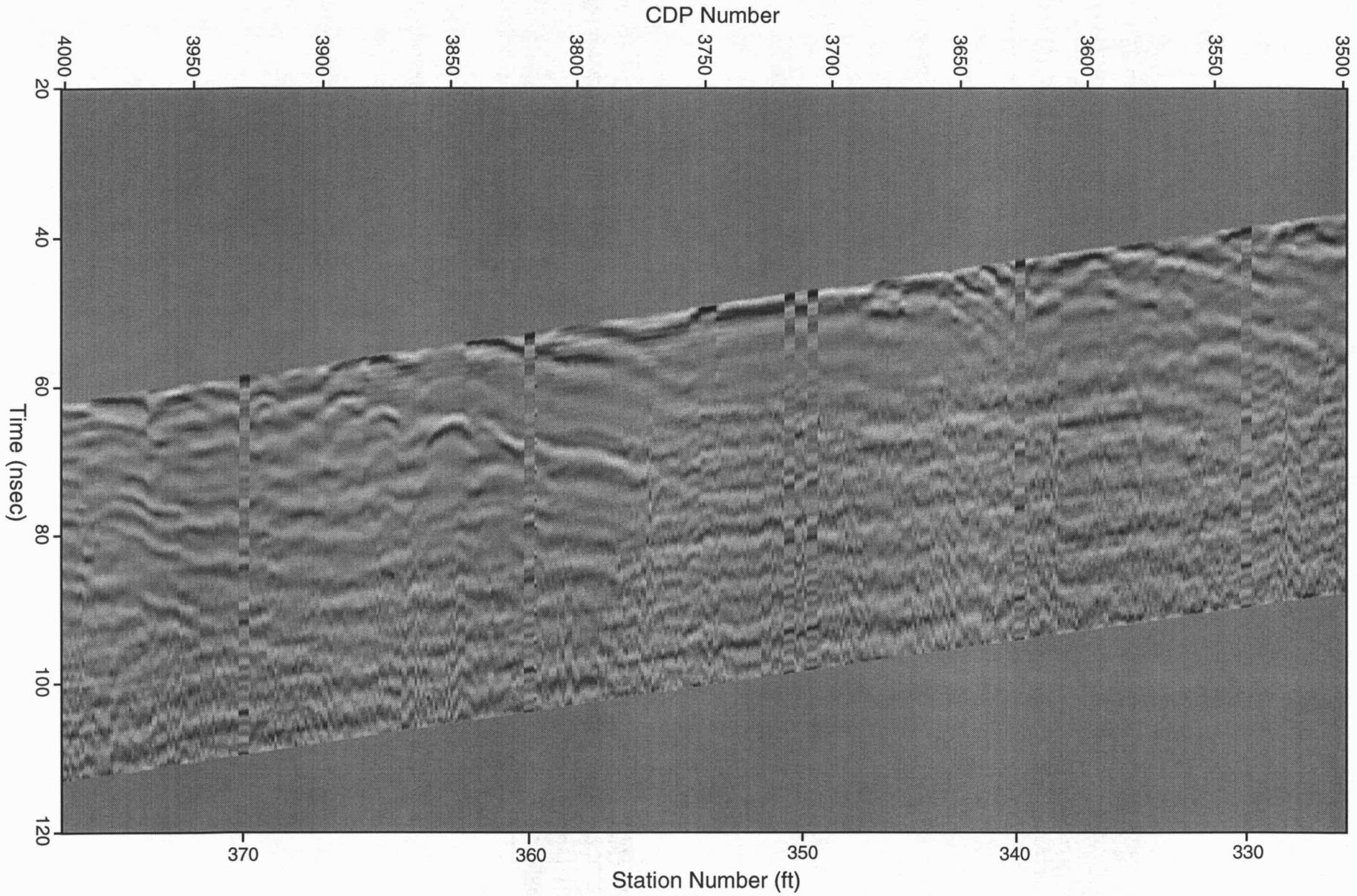

Figure 5h. Continuation of GPR profile from the I-70/I-435 interchange.

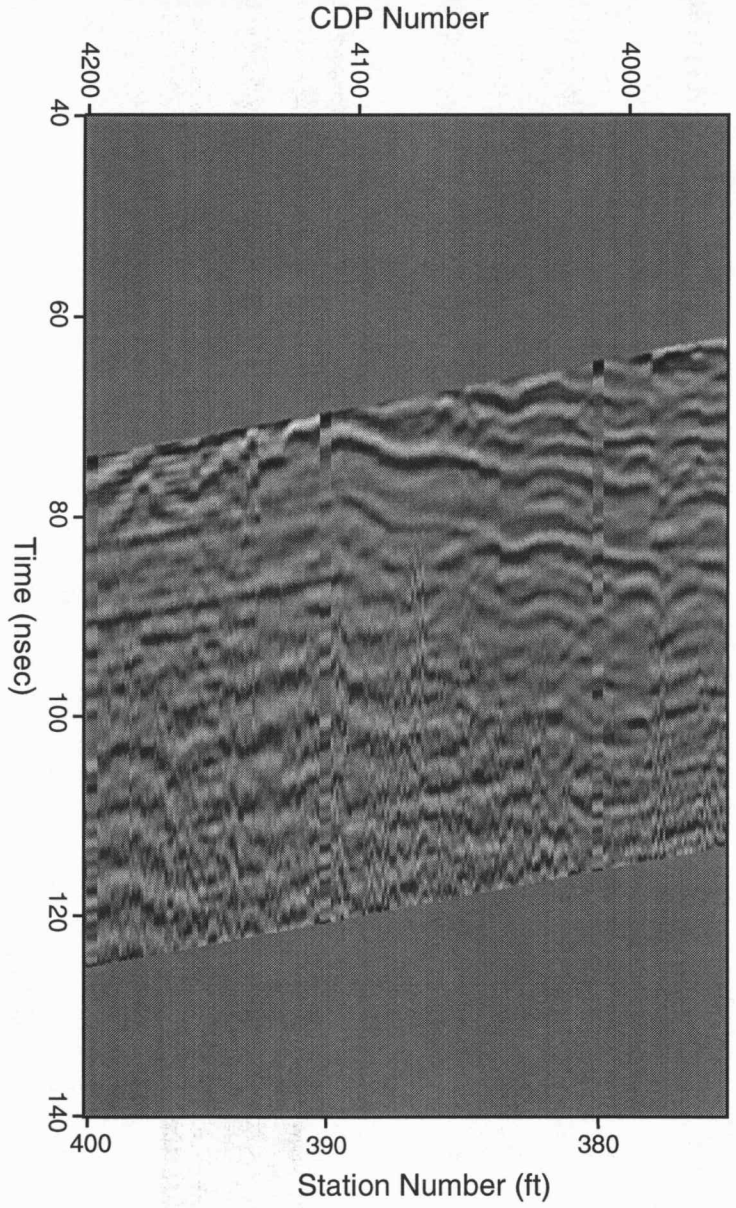

Figure 5i. Continuation of GPR profile from the I-70/I-435 interchange.

Figure 6a. Photograph of GPR stations 0-50.

Figure 6b. Photograph of GPR Stations 50-100.

Figure 6c. Photograph of GPR Stations 100-150.

Figure 6d. Photograph of GPR Stations 150-200.

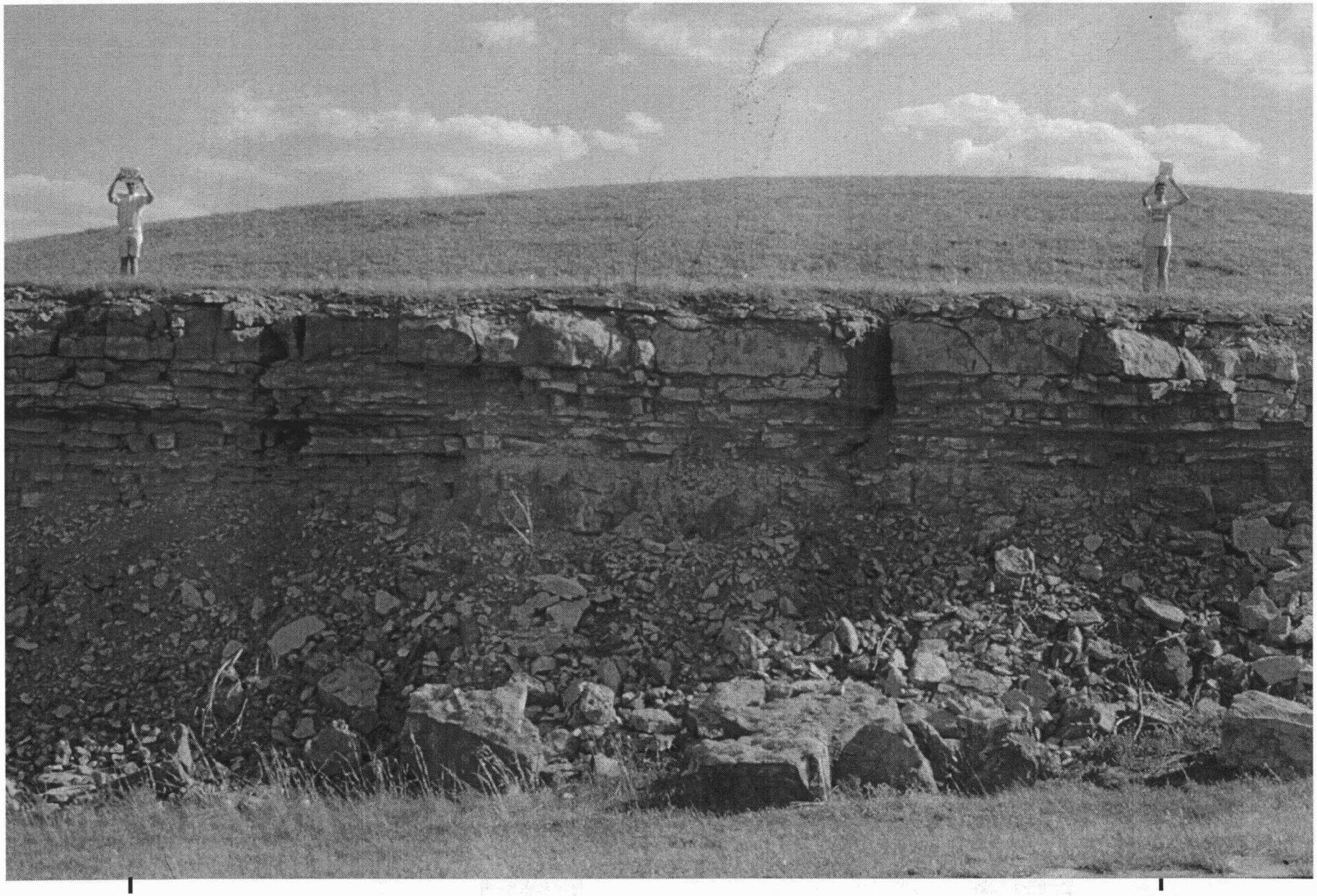

Figure 6e. Photograph of GPR Stations 200-250.

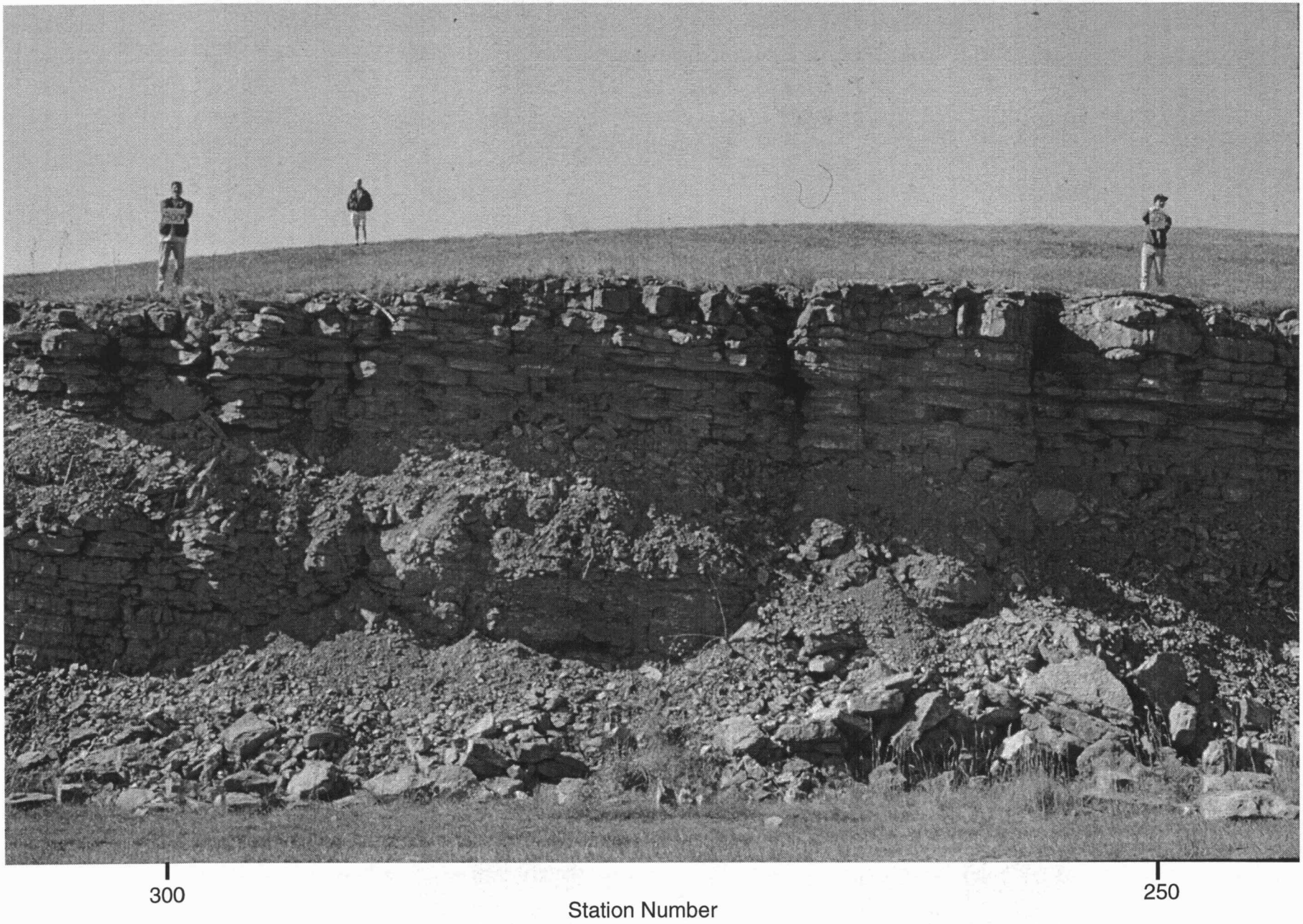

Figure 6f. Photograph of GPR Stations 250-300.

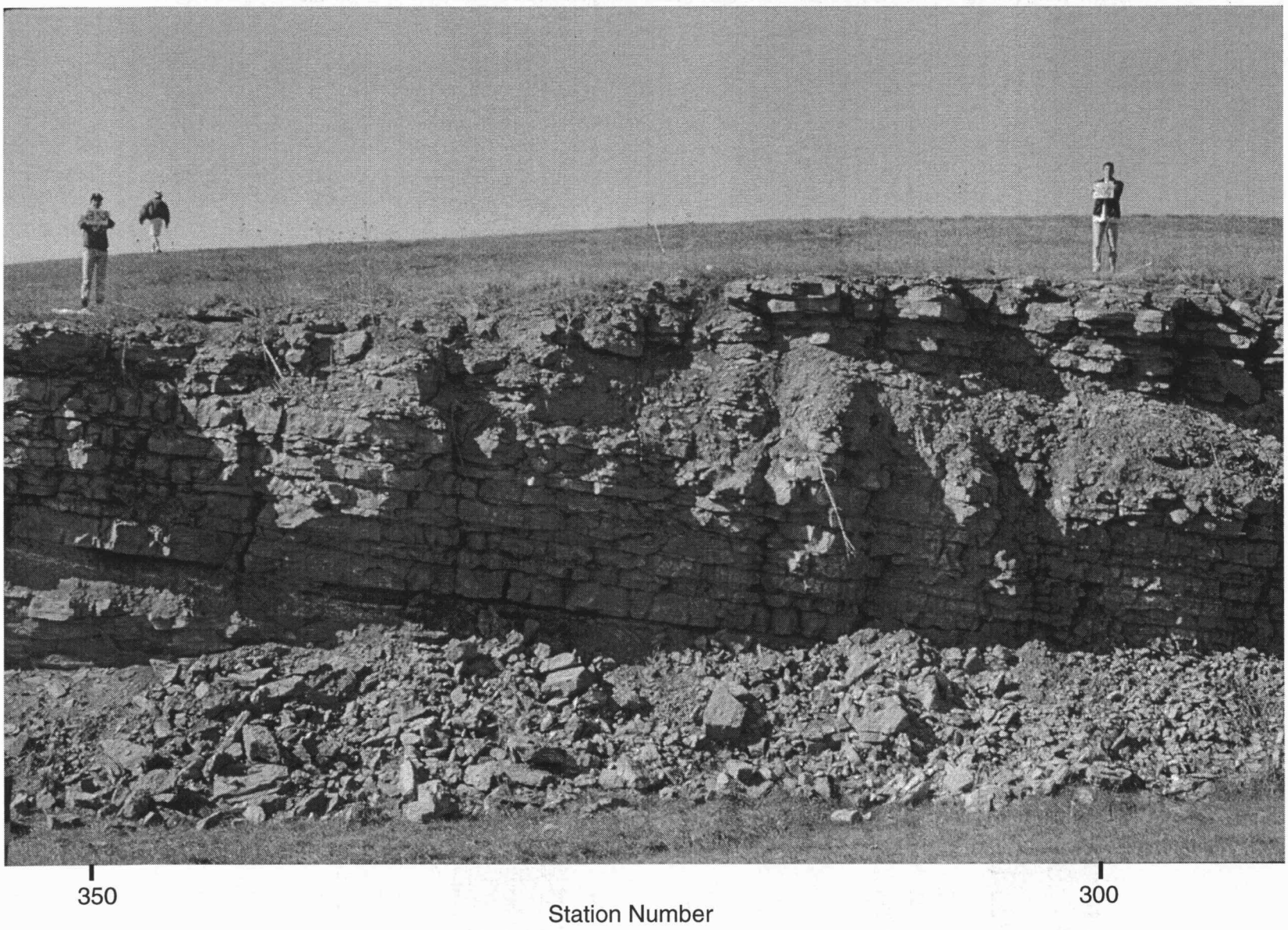

Figure 6g. Photograph of GPR Stations 300-350.

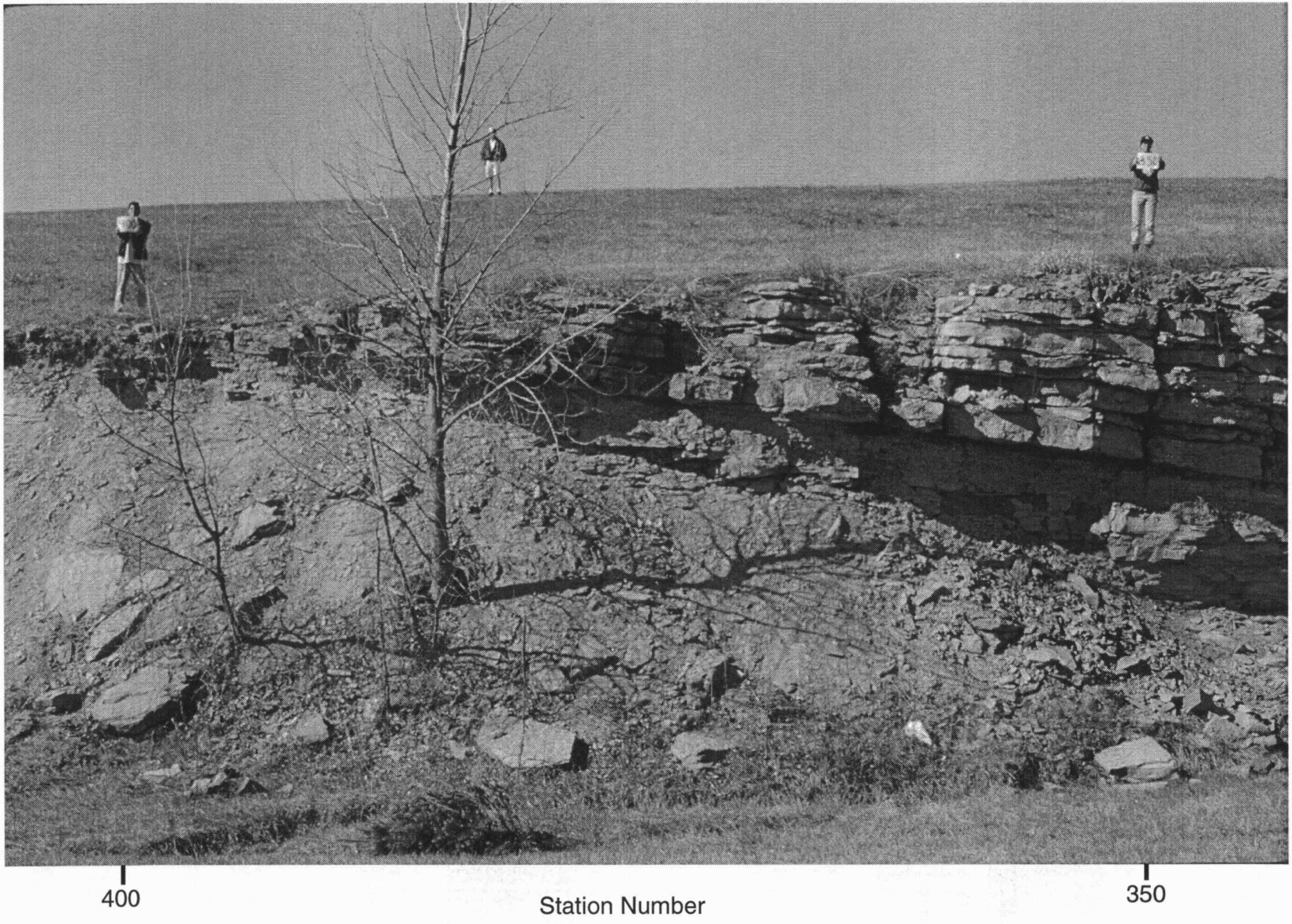

Figure 6h. Photograph of GPR Stations 350-400.